Realistic Magnetic Reconnection Processes and their Role in the Dynamics of Coronal Loops

Bruno Coppi

Massachusetts Institute of Technology

Coronal Loop Workshop VII
University of Cambridge, 21-23 July 2015

Magnetic Reconnection Processes

Recognized to be important in

- Space Physics
- Laboratory Plasmas for Fusion Research
- Solar Physics

and, by now, in

- High Energy Astrophysics

Related Remarks

- The onset and the evolution of reconnection events depend on the configuration (geometry) of the fields and flows in which these events take place.
- Examples of considered configurations are:
    - loops
    - tori
    - single X-point
    - double Y
    - neutral sheet

- What used to be a liability of reconnection, that of involving small scale distances should turn out to be an asset to explain the observed rapid variations of high energy radiation emission from a variety of objects
- Relevant surprise with the crossing of the Terminal Shock by the Voyager spacecraft

- Considered also for
    - Pulsar Nebulae (e.g. Crab; 5 PeV electrons)
    - Quasars
    - Blazars
    - Grazars
- Discovery of the direction of propagation of magnetic islands produced by reconnecting modes in high temperature (low collisionality) regimes
- This direction attributed to the phase velocity of the relevant reconnecting mode is that (unexpected) of the ion diamagnetic velocity. The only theoretical explanation based on introducing an "inductivity" involving the time evolution of the current density to break the "frozen-in-law".
- Numerous other surprises that deserve the analysis of relevant reconnection processes such as the
    - Discovery of two-tail configuration on the night side of Uranus, by the Voyager II mission (1985).

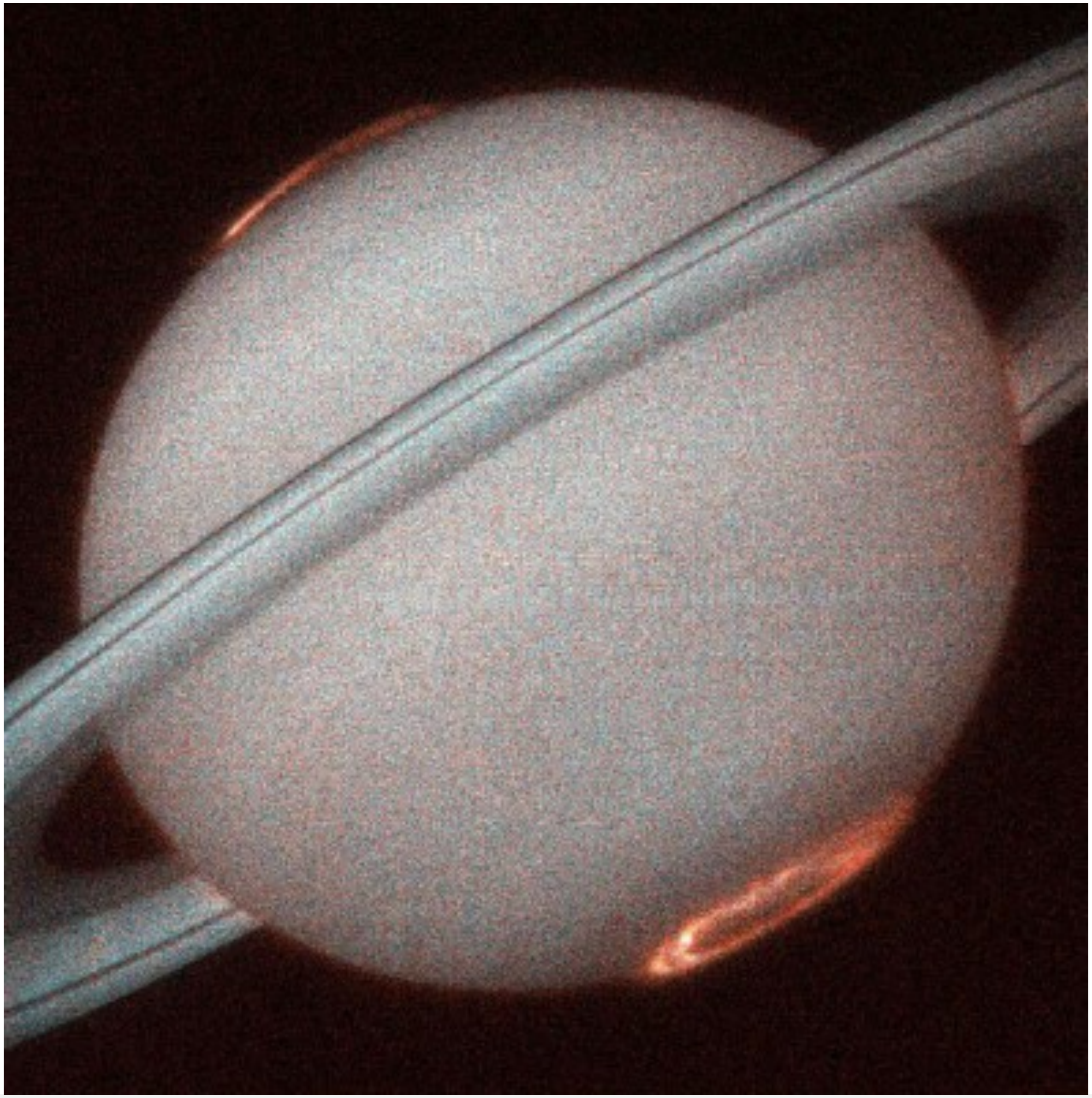

Hubble Space telescope photo in UV light showing Saturn's north and south ovals. Credit: NASA/ESA - See more at: http://astrobob.areavoices.com/tag/auroral-oval/#sthash.JTRVzgUS.dpuf

The northern auroral oval is centered on the north geomagnetic pole currently located in northern Canada. Credit: NASA - See more at: http://astrobob.areavoices.com/tag/auroral-oval/#sthash.JTRVzgUS.dpuf charge and momentum. They fell on the metal wall of the chamber and emitted light at the points of impact; this could be observed through a glass plate which had been fixed on the opposite side of the chamber with soft 'Araldite'. The position of protons and hydrogen molecular ions was always well defined on the chamber wall, and their deflexion due to magnetic field, thus determined, agreed within probable error of measurements with our theoretical calculations.

The field of the electromagnet was calibrated with a Grassot's fluxmeter within the pole pieces and outside, extending to the copper canal and the side walls of the analyser. The chamber, together with the accelerating column, was evacuated by a fast oil pump backed by a Kinney pump through a 'Freon' cold trap, and the pressure inside it was kept as low as 10^{-6} mm mercury during the experiments.

At an incident ion energy of 360 keV and with a suitable fixed magnetic field, well-defined spots could be seen on the metal wall of the analyser. These were due to singly and multiply charged copper ions, such as Cu^{+}, Cu^{2+}, Cu^{3+}, Cu^{4+} and Cu^{5+}, which were emitted from the canal surface by fast protons and molecular hydrogen ions. The spots due to Cu^{2+} ions overlapped with those due to incident ions causing their emission, but all other spots were well separated from one another, indicating that there was no appreciable energy spread among the emitted ions belonging to a particular group and entering the analyser. The energy and momentum of these ions, as calculated from the deflexion they experienced in the magnetic field, were in agreement, within experimental error, with equations (1) and (2). Copper ions carrying more than five charges were not detected within the energy range of the incident ions investigated. At an energy of 100 keV of the incident ions there were three spots, at 200 keV five, while at 360 keV all the aforementioned species of charges appeared. This made us believe that the efficiency of emission of ions and the multiplicity of their charge rise with energy of the incident beam.

We were not able to detect any ions of impurities which, it was suspected, might be present in the discharge tube of the radiofrequency ion source, and hence we believe that all the emitted Cu ions were due to single bi-particle elastic collisions of protons and hydrogen molecular ions with Cu atoms lying on the surface of the canal. There is some uncertainty as to the nature of one or two rather faint spots which occurred in the momentum spectrum (which was spread over a length of 10–11 cm). The only plausible explanation that we can offer is that they were formed due to multiply charged ions the positive charge of which was degraded during their flight in the trajectories in the magnetic field from the canal to the collector plate. No attempt was made to detect whether complex particles[3], for example of any compound of copper, were emitted in these experiments from copper surface. If they were, they overlapped with Cu ions.

The incident beam current on the copper canal and the thick metal disk which held it in position varied between 30 and 40 μamp, while the energy of the incident ions ranged between 100 keV and 360 keV in these experiments.

We thank His Excellency Nawab Malik Amir Mohammed Khan, Governor of West Pakistan, for his encouragement to our research, and Sir John Cockcroft for his interest in these experiments.

RAFI MOHAMMED CHAUDHRI
MUSTAFA YAR KHAN
M. MUNAWAR CHAUDHRI

High Tension and Nuclear Research Laboratory,
Church Road, Government College,
Lahore, West Pakistan.

[1] Datz, S., and Snoek, C., *Phys. Rev.*, **134**, A 347 (1964); *Proc. Sixth Intern. Conf. Ionization Phenomena in Gases* (Paris), **4** (7), 27 (1963).
[2] Chaudhri, R. M., Khan, M. Y., and Chaudhri, M. M., *Proc. Sixth Intern. Conf. Ionization Phenomena in Gases* (Paris), **4** (5), 21 (1963).
[3] McHugh, James A., and Sheffield, James C., *J. App. Phys.*, **35**, 512 (1964).

GEOPHYSICS

Role of Plasma Instabilities in Auroral Phenomena

RECENTLY it was proposed that plasma instabilities are responsible for the auroral precipitation of particles trapped inside the magnetosphere[1]. The entire event would be a two-step process, one which takes particles inside the magnetosphere and one which dumps the trapped particles. Responsible for the second step would be plasma micro-instabilities of the type outlined by Krall and Rosenbluth[2].

Against this view is the fact that the number of particles and the amount of energy contained inside the radiation belts are barely sufficient to supply one auroral event[3]. Moreover, micro-instabilities are not the most suitable ones for explaining gross plasma motion and can be inhibited by a number of factors[4], such as the presence of a shear in the magnetic field.

The necessity of overcoming these objections leads one to look for plasma macroscopic instabilities which exist in collisionless régimes and do not respect the constraint that particles move together with the lines of magnetic field. Instabilities of this nature may be suitable for explaining the first step, as they would allow potential energy stored in the magnetic field of the thermalized solar wind to be transferred into kinetic energy. This process could occur inside the magnetopause or on the corresponding nightside.

In order to avoid having to consider the trapping and dumping phase, it is proposed that the instability excites plasma waves and then accelerates particles according to a pattern of the type considered by Stix[5].

Although at the present stage it is difficult to identify one definite type of plasma instability as being responsible for the auroral process, I would mention that two classes of macroscopic collisionless instabilities have been investigated[6,7]. One of them[7] is related to the appearance of an electric field parallel to the lines of the magnetic field, so that the 'frozen-in law' does not hold, due to anisotropic pressure and ion gyro radius effects. The driving factor is a spatial gradient of the longitudinal electron pressure or a gradient of the density together with transverse pressure gradients. In the case when the equilibrium magnetic field has no shear, the growth rate of the instability is of the order:

$$\gamma \approx k \frac{p'_{e\parallel}}{\Omega\rho}$$

where k is the wave number transverse to the magnetic field, $p'_{e\parallel}$ the transverse gradient of the longitudinal electron pressure, ρ the mass density and Ω the ion gyrofrequency. Assuming typically that: $p'_{e\parallel}/\rho \approx v^2_{the}/R$, $R \approx 10^9$ cm, $v_{the} \approx 4\times10^7$ cm/sec, $B \approx 10^{-3}$ gauss, $k \approx 10^{-7}$ cm^{-1}, we obtain $\gamma \approx 10^{-1}$ sec^{-1}. For shorter wavelengths, that is $k \approx 10^{-5}$ cm^{-1}, the growth time becomes 10^{-1} sec, which seems to be consistent with the duration of burst of auroral X-rays observed recently[8].

I thank Drs. P. A. Sturrock and R. Wentworth for interesting discussions, and Drs. J. W. Chamberlain and J. I. Valerio for their comments. This work was supported by an Air Force Office of Scientific Research contract, *AF* 49(638)–1321.

BRUNO COPPI*

Institute for Plasma Research,
Stanford University, Stanford, California.

* On leave of absence at the University of California, San Diego, La Jolla.

[1] Chamberlain, J. W., *J. Geophys. Res.*, **68**, 5667 (1963).
[2] Krall, N., and Rosenbluth, M. N., *Phys. Fluids*, **6**, 254 (1963).
[3] Wentworth, R. (personal communication).
[4] Rosenbluth, M. N., in Report *CLM–M*21, 26 (Culham, 1963).
[5] Stix, T. H., Report *Matt*–219 (Princeton University, 1964).
[6] Coppi, B., *Physics Letters*, **11**, 226 (1964); **12**, 213 (1964).
[7] Coppi, B., Report *M.L.* 1278 (Stanford University, 1964).
[8] Anderson, K. A., and Milton, D. W., Report *UCB*–64/5 (University California, Berkeley, 1964).

JOURNAL OF GEOPHYSICAL RESEARCH VOL. 70, NO. 13 JULY 1, 1965

The Earth's Magnetic Tail[1]

NORMAN F. NESS

Goddard Space Flight Center
Greenbelt, Maryland

Abstract. Extensive measurements of the magnetic field of the earth at distances greater than approximately $7R_e$ (earth radii) have been performed by the Imp 1 satellite. These magnetic field measurements began on November 27, 1963, and ended on May 30, 1964. During this six-month interval the apogee-earth-sun angle in solar ecliptic coordinates decreased from 336° to 156°. The apogee of the satellite was $31.7R_e$, and the range of the magnetometers was between 0.25 and 300γ. This paper is concerned principally with the topology of the magnetic field within the magnetosphere and the position of both its boundary and the detached collisionless bow shock wave. The geomagnetic field is observed to trail out far behind the earth in the antisolar direction, thus forming a *magnetic tail.* Magnetic field strengths of approximately 10 to 30 γ are observed out to satellite apogee. The diameter of the magnetosphere at a distance of $30R_e$ behind the earth is found to be approximately $40R_e$. The direction of the field is parallel to the earth-sun line and in the antisolar direction below the solar magnetospheric equatorial plane and in the solar direction above this plane. A neutral surface separating antisolar directed fields in the southern hemisphere from solar directed fields in the northern hemisphere has been detected over a large area. This experimental result suggests the development of quantitative theories explaining the aurora, gegenschein, day-night asymmetry, and formation of the radiation belts. On the basis of a preliminary review of the data, it appears that the geomagnetic field trails out far behind the earth following the flow field of the solar plasma to a distance far beyond the orbit of the moon. No termination of the magnetic tail is detected or suggested by the data. Thus the earth can be compared to the nucleus of a comet, the radiation belts and co-rotating magnetosphere being the coma and the magnetic tail being the cometary tail.

Introduction. Detailed measurements of the earth's magnetic field at geocentric distances up to $31.4R_e$ (earth radii) have been made on the nighttime side of the earth by the Imp 1 satellite (Explorer 18). The most significant results of these measurements reveal the formation of an extended *magnetic tail* behind the earth caused by the interaction of the solar wind with the geomagnetic field. A magnetically neutral sheet has been discovered separating regions of oppositely directed magnetic fields in the magnetic tail. A direct relationship of these results to other satellite measurements and related terrestrial phenomena is strongly suggested. An expanded report on these experimental results and the substantiating data will be presented in the near future.

The magnetic field experiment instrumented for Imp 1 has already been discussed in a previous publication [*Ness et al.*, 1964] which should be consulted for a detailed description of the experiment and the initial results. This paper briefly discusses the results obtained from continued operation of the satellite for orbits 20 through 48, corresponding to the time interval February 9 to May 30, 1964. Successful operation of the satellite from November 27, 1963, to May 30, 1964, ended because of lack of adequate power from the solar paddle system. Until November 12, 1964, the satellite repetitively cycled in an under-voltage mode until the solar aspect angle changed to a more favorable value with respect to power output. From November 12 to December 18, 1964, the satellite has been successfully transmitting both rubidium vapor and flux-gate magnetometer data. However, these most recent data are not included in this paper.

Certain aspects of the satellite orbit are important in the understanding of the region of space mapped out during the first six months of operation of Imp 1. The orbit is highly elliptical

[1] Presented at Second Benedum Conference on Earth Magnetism, University of Pittsburgh, Pittsburgh, Pennsylvania, November 23, 1964.

DYNAMICS OF THE GEOMAGNETIC TAIL

B. Coppi, G. Laval, and R. Pellat
International Centre for Theoretical Physics, Trieste, Italy
(Received 13 January 1966)

In a paper recently published,[1] Ness has reported the experimental evidence of a magnetically neutral sheet behind the earth at a distance of (20-30)R_e (earth radii). This sheet separates regions of oppositely directed magnetic fields in the magnetic tail (Fig. 1). It has been proposed by Ness[1] and subsequent authors that the dynamics of this sheet may have an essential role in geomagnetic phenomena. This suggests as a model the analysis of the stability of a pinch containing a neutral sheet.[2] In fact, theory and laboratory experiments[3-5] clearly show that this configuration is violently unstable as it breaks up into separate pinches (Fig. 2), lying on the neutral sheet, which tend to repel each other. Considering the order of magnitude of the sheet thickness (600 km), and the energy of the electrons there contained, we see immediately that collisional effects (such as resistivity) cannot play a role in the dynamics of the neutral sheet. For this, we can take up the stability analysis of a collisionless pinch,[2,6] with the intention

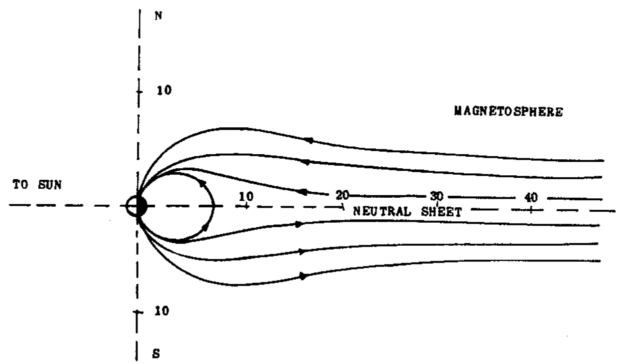

FIG. 1. Projection of magnetic field topology on noon-midnight meridian plane in the vicinity of the neutral sheet (unperturbed configuration). Distance in earth radii.

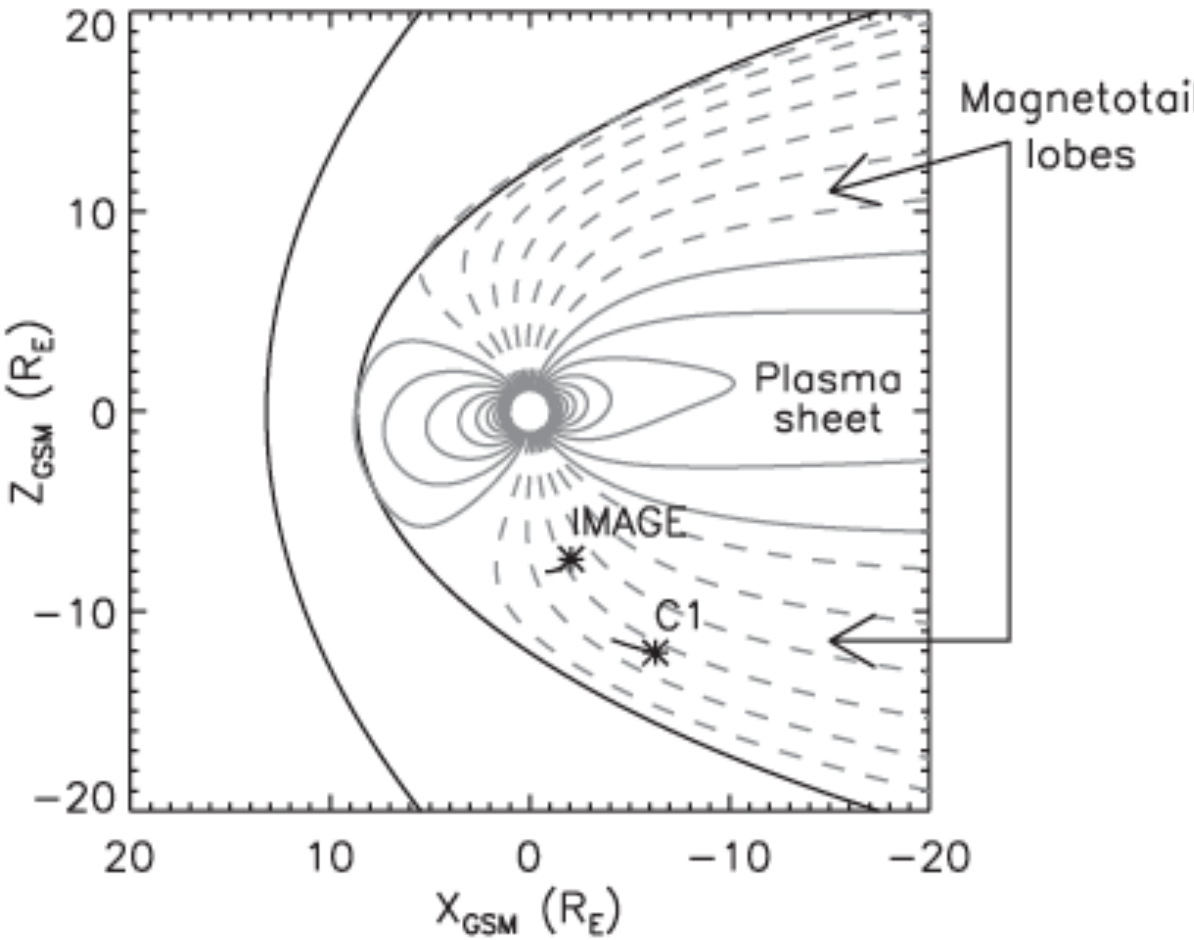

Fig. 1. Locations of Cluster 1 and Image spacecraft between 17:00 and 19:00 UT on 15 September 2005.
Sciencemag. Vol. 346bIssue 6216, 1507

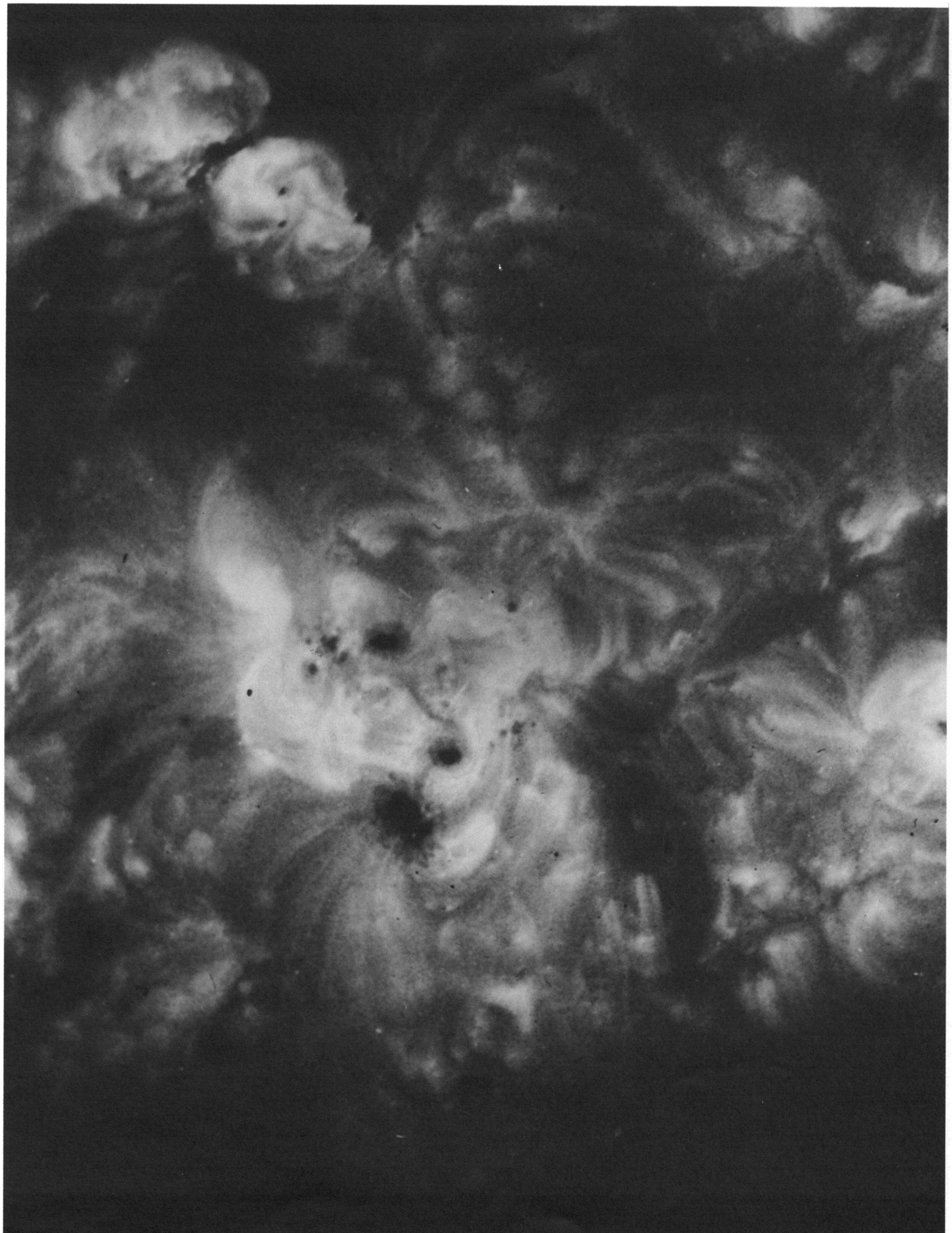

FIG. 1.—X-ray image of the solar corona obtained from a NASA sounding rocket on 1991 July 11. The X-ray corona is seen to consist of numerous long thin loops of hot plasma ($\approx 3 \times 10^6$ K) confined by the solar magnetic field.

BEAUFUMÉ, COPPI, & GOLUB (see 393, 397)

THE ASTROPHYSICAL JOURNAL, 393:396–408, 1992 July 1

CORONAL LOOPS: CURRENT-BASED HEATING PROCESSES

P. BEAUFUMÉ
Smithsonian Astrophysical Observatory; and C.E.N. Cadarache, D.R.F.C., bat. 513, St. Paul-lez-Durance, F13108 France

B. COPPI
Massachusetts Institute of Technology, Physics Department, Cambridge, MA 02139

AND

L. GOLUB
Harvard-Smithsonian Center for Astrophysics, 60 Garden Street, Cambridge, MA 02138
Received 1991 May 10; accepted 1992 January 7

ABSTRACT

A set of new experimental observations on the structure of the solar corona (Golub et al.) is used as input to the formulation of a theoretical model of magnetic field-related coronal heating processes. Field-aligned currents are assumed to be induced along coronal loops in thin current sheaths given that the rate of current density diffusion is relatively low. The excitation of instabilities involving magnetic reconnection is proposed to occur and convert the energy associated with the current-related magnetic field directly into particle energy. The estimated heating rate in this phase exceeds the energetic requirements of the loop and the heating process is envisioned as proceeding via short bursts corresponding to an intermittent disruption of the current sheath configuration.

Because of the relatively low transverse thermal conduction, only a small fraction of the loop volume is heated to a much higher temperature than the average value. This is consistent with the experimental observations of low filling factors of hot plasmas in coronal loops (published by Martens et al.) Thus the proposed model involves a repeated sequence of dynamic events taking into account the observed loop topology, the differential emission measure distribution in the 10^6–10^7 K range, the energy balance requirements in the loop, and the probable duty cycles involved in the heating process.

Subject headings: MHD — Sun: corona — Sun: magnetic fields

1. INTRODUCTION

The primary feature of the solar corona is its plasma temperature in excess of $\sim 10^6$ K, which thus radiates predominantly in the X-ray regime. Early studies used the assumption of homogeneity to derive the average properties of the solar atmosphere. However, progress in X-ray imaging techniques revealed that the corona is fundamentally inhomogeneous; for instance, Vaiana, Krieger, & Timothy (1973) identified "six classes of coronal structures observable in the X-ray photographs."

It was initially suggested that high temperature in the corona was maintained by dissipation of various waves originating in the convection zone, but Rosner et al. (1978a) and Golub et al. (1980) suggested that coronal heating is strongly correlated with a coupling of the magnetic structures to convective motions at the surface of the Sun. More recently, the arguments against the possibility of coronal heating by purely acoustic waves and showing the central role played by the magnetic field have been summarized in Ulmschneider (1991).

Parker (1990) emphasizes that once the question of the heat input is solved, the formation and sustainment of the corona follow in a simple way. Parker shows that the heat input raises the temperature of the gas and lets it expand upward; thermal conduction then heats the upper chromosphere and evaporation fills the so-formed corona. Equilibrium with the energy losses is finally reached, the density being controlled by the radiative losses ($\propto n_e^2$) and the temperature being limited by the conductive losses along the magnetic field lines ($\propto T^{7/2}$). However, the observed transverse scale sizes and local contrast factors of coronal loops are not easily explained.

Given the fact that theories of the solar corona may involve spatial scales below the available resolution as well as components of the magnetic field which are difficult to observe, assessing how well-founded a given model may be is a delicate matter. A large number of models, most of them static, have been proposed to explain the heating of the solar corona. It is beyond the scope of this paper to review the theoretical state of the art in coronal heating modeling (see Narain & Ulmschneider 1990 for a recent survey; also Kuperus, Ionson, & Spicer 1981).

It is now generally accepted that the configuration of coronal magnetic structures plays an important role in transforming the energy at the photospheric level into thermal energy in the corona. However, the details of this picture are not yet firmly established. Two types of motion can generate energy in the photosphere. Periodic motions of flux tubes produce MHD waves which propagate upward and may dissipate in the corona. Also, relatively slow motions of flux tubes may be considered as responsible for d.c. field–aligned electric currents induced in magnetic loops, which can lead to their heating. Thus, the theoretical work can be divided into two branches: wave theories and release of magnetic stresses via Joule heating in magnetic reconnection (see Hollweg 1990 for a review). The presence of large-amplitude Alfvén waves in the solar wind has been known for a long time, and waves seem to be necessary to explain the plasma heating that takes place in open magnetic regions. However, it is widely believed that electric currents are an important source of coronal heating in closed magnetic structure regions. This paper will focus on the latter possibility.

pressure and a higher magnetic field strength. Activity occurs within a wide range of parameters. In order to provide representative values, we shall use an artificial division of AR into long-lived versus short-lived features (Webb 1981); we shall also use values for a "typical" X-ray–bright point (XBP) even though these features are known to have a range of sizes. Little & Krieger (1977) give the following values for long-lived features (10–40 days): rise time: 1–5 days; temperature: $T \cong 2.5 \times 10^6$ K; and emission measure: $\mathrm{EM}_{\max} \sim 10^{48}$ cm^{-3} for $T > 10^6$ K; for short-lived features (1–5 days): rise time: several hours; temperature: $T \sim 1.8 \times 10^6$ K; and emission measure: $\mathrm{EM}_{\max} \sim 5 \times 10^{46}$ cm^{-3}; and for XBP (<1 day): temperature: $T \sim 1.6 \times 10^6$ K; emission measure: $\mathrm{EM}_{\max} \sim 2 \times 10^{46}$ cm^{-3}.

2.1.2. *Coronal Magnetic Field*

The solar photospheric and chromospheric magnetic field can be measured using the Zeeman effect ("magnetogram"), which is of fundamental importance for studying the outer atmosphere. However, it is not in general possible to measure magnetic fields in the corona because, for the Zeeman shift to be detectable in XUV coronal lines, it would be necessary that $B \approx T^{1/2}\lambda^{-1} \approx 4 \times 10^5$ G (Dere & Mason 1981), which is much higher than has been observed even in sunspots. Thus, extrapolations are needed to get the coronal part. It is found that simple potential extrapolations of the photospheric magnetic fields, based on the observed line-of-sight component derived from circular polarization, often yield a coronal field geometry similar to that of the observed X-ray structures (see Poletto et al. 1975).

We point out that the magnetic field of current carrying loops is not a potential field. All three components of the photospheric magnetic field are now available by measuring linear as well as circular polarizations ("vector magnetogram") and extrapolations are occasionally done. From these, departures from potential configurations, indicating the presence of currents, have been observed with moderate spatial resolution (2".5–5"). Major deviations are limited to spatially localized regions and are often associated with the occurrence of flare events (Hagyard et al. 1984).

2.2. *Loop Parameters*

Recent missions such as *Skylab* or *SMM* permitted the study of a large number of nonflaring ARs and the determination of their fundamental parameters (see Orrall 1981). Extensive observations show that there is not a single set of parameters for coronal loops but a rather wide range of values, in particular as far as the geometry and the brightness of the loops are concerned.

2.2.1. *Geometry*

The recent pictures of the corona given by the NIXT telescope in the soft X-ray range offer very high spatial resolution (1") and reveal that coronal loops are thinner than was previously thought. These new results are available from NIXT, a sounding rocket payload utilizing multilayer coating for enhanced soft X-ray reflectivity (Golub et al. 1990); an example of the new data is shown in Figure 1. After examination of the new imaging data, we take as the basis for our calculations an ideal cylindrical loop with a ratio between the half-length L (from a footpoint to the top) and the minor radius a (the radius of the loop) varying from $a/L = 0.04$ for compact AR loops down to 0.01 for large-scale structures (see Fig. 2). This inverse

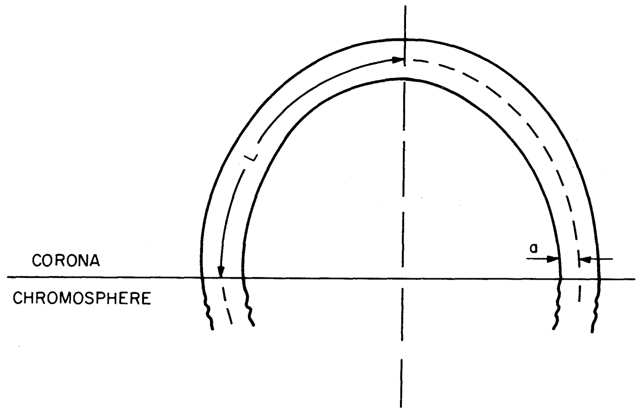

FIG. 2.—Geometry of a cylindrical loop. L is the length from apex to footpoint, and a is the cross-sectional radius.

aspect ratio is substantially lower than previous estimates, but is taken directly from the new imaging data. Coronal loop dimension measured from a number of X-ray pictures lie in the following ranges:

$$2 \times 10^9 \leq L_{[\mathrm{cm}]} \leq 2 \times 10^{10}$$
$$5 \times 10^7 \leq a_{[\mathrm{cm}]} \leq 4 \times 10^8 .$$

2.2.2. *Thermal Characteristics*

The average temperature along the line of sight can be derived from the flux ratio of two different coronal emission lines (Vaiana et al. 1973). A number of observations and theoretical considerations allow us to establish some characteristic thermal properties for the coronal loops:

1. Along the magnetic lines, loops are mainly isothermal because of the high coefficient of thermal conduction in that direction, with sharp transition zone gradients at the ends (see Webb 1981).

2. In the radial direction, the thermal conduction is limited by the cross-field coefficient, which is much lower than the longitudinal coefficient.

The coronal loops are seen to consist of two groups (see Vaiana & Rosner 1978):

1. The brighter hot loops ($T > 2 \times 10^6$ K) are low-lying (up to 2×10^9 cm) and have a duration of several days, at least as regards the overall configuration. Their footpoints are in the area of strong or changing magnetic field, with a correlation between brighter loops and enhanced chromospheric emission. In the hot loops, hydrostatic equilibrium prevails, the loop height is smaller than the pressure scale height, and there is no clear evidence for mass flows inside the loop.

2. The fainter cool loops ($T < 10^6$ K) are longer, thinner, less stable, less numerous, and shorter-lived. There is some evidence for plasma motions in cool loops by Doppler shift measurements on *SMM* (*Solar Maximum Mission*) (see Kopp et al. 1985), and Foukal (1978) has indicated that flows must be invoked in order to explain the great height to which these loops sometimes extend.

No obvious spatial relationship appears between the two sets of loops (Cheng 1980; Webb 1981). It is to be noted that within a factor of 2 or 3, the solar corona outside of flares is essentially at a uniform temperature around 2–3 $\times 10^6$ K (Golub et al. 1980; Cheng 1980), except for small amounts of very hot plasma. In active regions Pye et al. (1978) showed that

3. Thermal energy transport across the magnetic field lines is locally enhanced by disruption of the current sheath, and heat diffuses across the loop. This input of energy may lead to an evaporation process if the time scales are adequate: as a consequence of high thermal conduction along magnetic field lines the chromospheric material at the loop footpoints is heated up, and evaporates into the corona (Kuin & Martens 1982). This leads to a density increase which induces brightness variability since the latter is proportional to n_e^2. The resulting turbulence subsides and the cycle restarts with phase 1.

Dynamical processes which are all simultaneously happening on similar time scales are conduction of energy along the magnetic field lines leading to chromospheric evaporation; disruption of the current sheath and redistribution of the thermal energy; and formation of observable line emission by microscopic atomic processes. Because all these processes occur on time scales of 10–100 s, a detailed evaluation of the observable signature of the proposed sequence is difficult to carry out. High-resolution X-ray observations of the corona, photospheric vector-magnetograms, and emission measure analysis, combined with spectroscopic measurements in order to detect small amounts of very hot plasma in coronal loops, and the relevant filling factors, will be necessary in order to carry the model we have proposed to a further degree of development.

This work has been supported in part by NASA grant NAGW-112 to the Smithsonian Institution (L. G.), by the Smithsonian Predoctoral Fellowship Program (P. B.), and by the Air Force Geophysics Laboratory (APL contract 602220-0) (B. C.) We thank Marc Herant and Francie Pardo for assistance with the NIXT data reduction and Aad van Ballegooijen for helpful comments on the manuscript.

REFERENCES

Cheng, C. C. 1980, ApJ, 238, 743
Coppi, B. 1963, in Propagation and Instabilities in Plasmas, ed. W. I. Futterman (Stanford, CA: Stanford Univ. Press), 70
———. 1964, Phys. Lett., 11, 226
Coppi, B., & Detragiache, P. 1990, Phys. Rev. Lett., submitted
Coppi, B., & Friedland, A. B. 1971, ApJ, 169, 379
Coppi, B., Galvao, R., Pellat, R., Rosenbluth, M. N., & Rutherford, P. H. 1976a, Soviet J. Plasma Phys., 2, 533
Coppi, B., Laval, G., Pellat, R., & Rosenbluth, M. N. 1966, Nucl. Fusion, 6, 261
Coppi, B., Pegoraro, F., Pozzoli, R., & Rewoldt, G. 1976b, Nucl. Fusion., 16(2), 309
Coppi, B., & Rem, J. 1972, Sci. Am., 227, 65
De Bruynes, P., & Hood, A. W. 1989, Sol. Phys., 123, 241
De Jager, C., Machado, M. E., Schadee, A., Strong, K. T., Svestka, Z., Woodgate, B. E., & Van Tend, W. 1983, Sol. Phys., 84, 205
Dere, K. P. 1982, Sol. Phys., 75, 189
Dere, K. P., & Mason, H. 1981, in Solar Active Regions, ed. F. O. Orall (Boulder: Colorado Associated University Press), 157
Foukal, P. 1978, ApJ, 223, 1046
Gary, G. A., Moore, R. L., Hagyard, M. J., & Haisch, B. M. 1987, ApJ, 314, 782
Golub, L., Hartquist, T. W., & Quillen, A. C. 1989, Sol. Phys., 122, 245
Golub, L., Herant, M., Kalata, K., Lovas, I., Nystrom, G., Pardo, F., Spiller, E., & Wilczynski, J. 1990, Nature, 344, 842
Golub, L., Maxson, C., Rosner, R., Serio, S., & Vaiana, G. S. 1980, ApJ, 238, 343
Hagyard, M. J., Smith, J. B., Jr., Teuber, D., & West, E. A. 1984, Sol. Phys., 91, 115
Haisch, B. M., Bruner, M. E., Hagyard, M. J., & Bonnet, R. M. 1986, ApJ, 300, 428
Haisch, B. M., Strong, K. T., Harrison, R. A., & Gary, G. A. 1988, ApJS, 68, 371
Hollweg, J. V. 1990, Comput. Phys. Rep., 12, 205
Hood, A. W., & Priest, E. R. 1979, Sol. Phys., 64, 303
Kaplan, S. A., & Tsytovich, V. A. 1973, Plasma Astrophysics (London: Pergamon)
Kopp, R. A., Poletto, G., Noci, G., & Bruner, M. 1985, Sol. Phys., 98, 91
Krall, K. R. 1977, Sol. Phys., 55, 455
Kuin, N. P. M., & Martens, P. C. H. 1982, A&A, 108, L1
Kuperus, M., Ionson, J. A., & Spicer, D. S. 1981, ARA&A, 19, 7
Levine, R. H., & Pye, J. P. 1980, Sol Phys., 66, 39
Levine, R. H., & Withbroe, G. L. 1977, Sol. Phys., 51, 83
Lin, R. P., Schwartz, R. A., Kane, S. R., Pelling, R. M., & Hurley, K. C. 1984, ApJ, 283, 421
Little, S. J., & Krieger, A. S. 1977, BAAS, 9, 341
Martens, P. C. H., Van Den Oord, G. H. J., & Hoyng, P. 1985, Sol. Phys., 96, 253
Narain, U., & Ulmschneider, P. 1990, Space Sci. Rev., 54, 377
Orrall, F. O., ed. 1981, Solar Active Regions (Boulder: Colorado Associated Univ. Press)
Parker, E. N. 1972, ApJ, 174, 499
———. 1988, ApJ, 330, 474
———. 1990, Adv. Space Res., 10(9), 17
Priest, E. R. 1982, Solar Magnetohydrodynamics (Dordrecht: Reidel)
Poletto, G., Vaiana, G. S., Zombeck, M. V., Krieger, A. S., & Timothy, A. F. 1975, Sol. Phys., 44, 83
Pye, J. P., Evans, K. D., Hutcheon, R. J., Gerassimenko, M., Davis, J. M., Krieger, A. S., & Vesecky, J. F. 1978, A&A, 65, 123
Raymond, J. C., & Foukal, P. 1982, ApJ, 253, 323
Rosner, R., Golub, L., Coppi, B., & Vaiana, G. S. 1978a, ApJ, 222, 317
Rosner, R., Tucker, W. H., & Vaiana, G. S. 1978b, ApJ, 220, 643
Schadee, A., De Jager, C., & Svestka, Z. 1983, Sol. Phys., 89, 287
Sheeley, N. R., & Golub, L. 1979, Sol. Phys., 63, 119
Spicer, D. S. 1981, Sol. Phys., 70, 149
———. 1991, in Mechanisms of Chromospheric and Coronal Heating, ed. P. Ulmschneider, E. R. Priest, & R. Rosner (Heidelberg: Springer), 547
Spitzer, L. 1962, Physics of Fully Ionized Gases (New York: Interscience)
Title, A. M., Tarbel, T. D., Topka, K. P., Fergusson, S. H., Shine, R. A., & the SOUP Team. 1989, ApJ, 336, 475
Tucker, W. H. 1973, ApJ, 186, 285
Ulmschneider, P. 1991, in Mechanisms of Chromospheric and Coronal Heating, ed. P. Ulmschneider, E. R. Priest, & R. Rosner (Heidelberg: Springer), 328
Vaiana, G. S., Krieger, A. S., & Timothy, A. F. 1973, Sol. Phys., 32, 81
Vaiana, G. S., & Rosner, R. 1978, ARA&A, 16, 393
van Ballegooijen, A. A. 1986, ApJ, 311, 1001.
———. 1990, in Cool Stars, Stellar Systems and the Sun, ed. G. Wallerstein (ASP Conf. Ser., 9), 15
Webb, D. F. 1981, in Solar Active Regions, ed. F. O. Orall (Boulder: Colorado Associated Univ. Press), 165
Wesson, J. 1986, Tokamaks (Oxford: Clarendon Press)

THE ASTROPHYSICAL JOURNAL, 222:317–332, 1978 May 15

HEATING OF CORONAL PLASMA BY ANOMALOUS CURRENT DISSIPATION

R. ROSNER AND L. GOLUB
Harvard-Smithsonian Center for Astrophysics
B. COPPI
Massachusetts Institute of Technology
AND
G. S. VAIANA
Harvard-Smithsonian Center for Astrophysics; and Osservatorio Astronomico di Palermo (Italy)
Received 1977 September 12; accepted 1977 November 22

ABSTRACT

We show that the observed high temperature and inhomogeneous structure of the solar corona, as well as the long-term spatial and temporal evolution of coronal features, is economically explained by *in situ* heating of the coronal plasma via anomalous current dissipation. The basic geometrical structure is a loop configuration heated by nearly field-aligned currents occupying a small fraction of the total loop volume. Energy is transferred from the turbulent convective zone and photosphere, where $\beta \gtrsim 1$, into the low-β corona via the magnetic fields which link the two regimes. The coronal currents are generated initially by relaxation of emerging magnetic flux to the nearly force-free configuration, and subsequent quasi-steady deposition of energy is achieved via induction processes arising from the continual transfer of azimuthal flux to the corona and from direct generation of electric fields along the flux tube by subphotospheric changes in flux linkage. Laboratory experiments show that the current filamentation necessary for this model can occur if the effective resistivity and radiative losses are strongly temperature dependent, as is the case in the solar corona. As a result, local temperature increases lead, via a regenerative process, to further temperature enhancement; the relative ineffectiveness of cross-field thermal transport leads to well-localized channels of current flow.

Subject headings: hydrodynamics — plasmas — Sun: corona

I. INTRODUCTION

The advent of high-resolution soft X-ray imaging has in recent years been responsible for a radical readjustment in our understanding of the nature of the inner corona. The early view of the corona as amorphous and generally unstructured, with streamers, coronal condensations, and the like providing only occasional and incidental structuring, has been replaced by a picture of the corona as dominated by a vast hierarchy of structures: active regions consisting of closed, compact loops; larger interconnecting loops between active regions, coronal holes, filament cavities, bright points, and many other features (cf. Van Speybroeck, Krieger, and Vaiana 1970; Vaiana, Krieger, and Timothy 1973). Virtually all of these observed structures can be directly linked to solar magnetic fields (Krieger, Vaiana, and Van Speybroeck 1971; Pneuman 1973; McIntosh *et al.* 1976); the usual interpretation is that the observed highly inhomogeneous nature of the inner corona finds its cause in the inhomogeneous nature of magnetic flux eruption through the solar photosphere.

Coronal heating theory is too extensive to be reviewed here (cf. Athay 1976). Progress in this area has traditionally been inhibited by the lack of sufficiently detailed plasma diagnostics on the observational side. This problem is compounded by the fact that the coronal energy requirement for balancing radiative losses is only a small fraction of the energy budget of the solar atmosphere (Athay 1976); therefore only a very modest and consequently difficult-to-detect contribution from several possible energy sources—such as acoustic noise generated by convective motions or magnetic fields emerging from the solar interior—could account for the coronal energy budget.

These uncertainties have been alleviated to some extent by the advent of spatially resolved diagnostic information, such as that provided by imaging X-ray telescopes (cf. Vaiana *et al.* 1977). The latter in particular have permitted the determination of, for example, the temporal and spatial distribution of the coronal plasma energy density, temperature, and emission measure along the line of sight (Landini *et al.* 1975; Davis *et al.* 1975; Kahler 1976). Consequently there now exist considerably more stringent constraints upon heating models; it is no longer obvious how coronal structures characterized by magnetic field strengths, energy densities, and scale sizes varying over many orders of magnitudes are to be maintained at coronal temperatures.

We intend to show that there exist heating mechanisms which connect the observed radiative properties of the inner corona in a simple way to the underlying

Note that for coronal loops, $\bar{p}$ refers to the average pressure difference between the loop interior and the ambient plasma. Typical values for the relevant parameters ($\bar{p} \sim 0.2$ dyn cm^{-2}, $a/R_0 \sim \frac{1}{3}$–1/10, $B_{p_0} \sim 10^2$–3×10^2 gauss) lead to the inequality

$$2 \text{ gauss} \ll B_{p_0} < 10\text{–}10^2 \text{ gauss}\,. \tag{A19}$$

Equations (A18) and (A19) are noteworthy in that they show the plasma β defined by the *poloidal* field component—not the toroidal component—to significantly constrain the possibilities for a force-free geometry.

REFERENCES

Anzer, U. 1968, *Solar Phys.*, **3**, 298.
Athay, R. G. 1976, *The Solar Chromosphere and Corona; Quiet Sun* (Dordrecht: Reidel).
Biskamp, D., and Horton, W. 1975, *Phys. Rev. Letters*, **35**, 39.
Cap, F. F. 1976, *Handbook on Plasma Instabilities* (New York: Academic Press).
Coppi, B. 1975, *Ap. J.*, **195**, 545.
Coppi, B., and Friedland, A. B. 1971, *Ap. J.*, **169**, 379.
Coppi, B., and Rem, J. 1972, *Sci. Amer.*, **227**, 65.
Cowling, T. G. 1946, *M.N.R.A.S.*, **106**, 446.
———. 1976, *Magnetohydrodynamics* (Bristol: Adam Hilger).
Davis, J. M., Gerassimenko, M., Krieger, A. S., and Vaiana, G. S. 1975, *Solar Phys.*, **45**, 393.
Foukal, P. 1976, *Ap. J.* (*Letters*), **203**, L145.
Frankenthal, S. 1977, *Ap. J.* (*Letters*), **215**, L131.
Furth, H. P., Rosenbluth, M. N., Rutherford, P. H., and Stodick, W. 1970, *Phys. Fluids*, **13**, 3020.
Galeev, A. A., Rosner, R., Serio, S., and Vaiana, G. S. 1978, in preparation.
Gary, S. P., and Paul, J. W. M. 1971, *Phys. Rev. Letters*, **26**, 1097.
Gerassimenko, M., Nolte, J. T., and Petrasso, R. D. 1976, *Solar Phys.*, **48**, 121.
Gold, T. 1964, *AAS–NASA Symposium on Physics of Solar Flares*, ed. W. Hess (NASA SP-50), p. 389.
Golub, L., Krieger, A. S., Silk, J. K., Timothy, A. F., and Vaiana, G. S. 1974, *Ap. J.* (*Letters*), **189**, L93.
Hamberger, S. M. 1975, *Survey Lectures*, Conf. Proc. 2d Intl. Congr. Waves and Instabilities in Plasmas, Innsbruck, Austria, ed. G. Auer and F. Cap.
Hamberger, S. M., and Jancarik, J. 1970, *Phys. Rev. Letters*, **25**, 999.
———. 1972, *Phys. Fluids*, **15**, 825.
Hamberger, S. M., Jancarik, J., and Sharp, L. F. 1969, 9th Intl. Congr. Phenomena in Ionized Gases, Contributed Papers, Bucharest, Roumania, p. 570.
Hamberger, S. M., Jancarik, J., Sharp, L. E., Aldcroft, D. A., and Wetherell, A. 1971, *Proc. 4th International Conference on Plasma Physics and Controlled Nuclear Fusion Research*, Madison, 1971 June, Vol. **2**.
Heyvaerts, J. 1974, *Solar Phys.*, **38**, 419.
Kadomtsev, B. B. 1966, *Rev. Plasma Phys.*, **2**, 153.
Kahler, S. 1976, *Solar Phys.*, **48**, 255.
Kaplan, S. A., and Tsytovich, V. N. 1973, *Plasma Astrophysics* (Oxford: Pergamon Press).
Krall, N. A., and Trivelpiece, A. W. 1973, *Principles of Plasma Physics* (New York: McGraw-Hill).
Krieger, A. S., DeFeiter, L. D., and Vaiana, G. S. 1976, *Solar Phys.*, **47**, 117.
Krieger, A. S., Paolini, F., Vaiana, G. S., and Webb, D. 1972, *Solar Phys.*, **22**, 150.
Krieger, A. S., Vaiana, G. S., and Van Speybroeck, L. P. 1971, in *Proc. IAU Symposium No. 43*, *Solar Magnetic Fields*, ed. R. Howard (Dordrecht: Reidel), p. 397.
Krieger, A. S., Vaiana, G. S., Van Speybroeck, L. P., Zehnpfennig, T., and Zombeck, M. V. 1970, *Bull. APS*, **15**, 612.
Landini, M., Monsignori-Fossi, B. C., Krieger, A. S., and Vaiana, G. S. 1975, *Solar Phys.*, **44**, 69.
Levine, R. H. 1974*a*, *Ap. J.*, **190**, 447.
———. 1974*b*, *Ap. J.*, **190**, 457.
Levine, R. H., and Altschuler, M. D. 1974, *Solar Phys.*, **36**, 345.
McIntosh, P. S., Krieger, A. S., Nolte, J. T., and Vaiana, G. S. 1976, *Solar Phys.*, **49**, 57.
Parker, E. N. 1972, *Solar Terrestrial Relations*, Conf. Proc. Calgary, Alberta, p. 1.
———. 1974, *Ap. J.*, **191**, 245.
———. 1975, *Ap. J.*, **201**, 494.
———. 1976, *Ap. Space Sci.*, **44**, 107.
Parkinson, J. H. 1973, *Solar Phys.*, **28**, 487.
Pneuman, G. W. 1973, *Solar Phys.*, **28**, 247.
Poletto, G., Vaiana, G. S., Zombeck, M. V., Krieger, A. S., and Timothy, A. F. 1975, *Solar Phys.*, **44**, 83.
Pye, J. P., Evans, K. D., Hutcheon, R. J., Gerassimenko, M., Davis, J. M., Krieger, A. S., and Vesecky, J. F. 1978, in preparation.
Rosner, R., Tucker, W. H., and Vaiana, G. S. 1978, *Ap. J.*, in press.
Sagdeev, R. Z. 1967, *Proc. Symp. Appl. Math.*, **18**, 281.
Shafranov, V. D. 1966, *Rev. Plasma Phys.*, **2**, 103.
Spitzer, L. 1962, *Physics of Fully Ionized Gases* (2d ed.; New York: Interscience).
Sturrock, P. A. 1972, *Solar Terrestrial Relations*, Conf. Proc. Calgary, Alberta, p. 63.
Svestka, Z. 1976, *Solar Flares* (Dordrecht: Reidel).
Tucker, W. H. 1973, *Ap. J.*, **186**, 285.
Tucker, W. H., and Koren, M. 1971, *Ap. J.*, **168**, 283.
Uchida, Y., and Sakurai, T. 1977, *Solar Phys.*, **51**, 413.
Vaiana, G. S., Krieger, A. S., and Timothy, A. F. 1973, *Solar Phys.*, **32**, 81.
Vaiana, G. S., Van Speybroeck, L. P., Zombeck, M. V., Krieger, A. S., Silk, J. K., and Timothy, A. F. 1977, *Space Sci. Instr.*, **3**, 19.
Van Speybroeck, L. P., Krieger, A. S., and Vaiana, G. S. 1970, *Nature*, **227**, 818.
Vasil'eva, A. N., Grishina, I. A., Pis'mennyi, V. D., and Rakhimov, A. T. 1972, *JETP Letters*, **15**, 433.
Vasyliunas, V. M. 1973, *Rev. Geophys. Space Phys.*, **13**, 303.
Withbroe, G. L. 1975, *Solar Phys.*, **45**, 301.

B. COPPI: Massachusetts Institute of Technology, Cambridge, MA 02139

L. GOLUB, R. ROSNER, and G. S. VAIANA: Harvard College Observatory, 60 Garden Street, Cambridge, MA 02138

Magnetic Reconnection in Plasmas with Inhomogeneous and Anisotropic Temperatures

Symmetric Current Sheet

$$\mathbf{B} = B_0 \mathbf{e}_z + B_y(x)\mathbf{e}_y$$

$$B_y = \text{odd function of } x \text{ (scale } \Delta_c\text{)}$$

Central Reconnection

$$\hat{B}_x = \tilde{B}_x(x,t)\exp(ik_y y)$$

$$k_y B_y = 0 \text{ for } x = 0$$

$$\tilde{B}_x(x,t) \text{ even function of } x$$

$$\tilde{B}_x(x=0,t) \neq 0$$

Lateral Reconnection

$$\hat{B}_x = \tilde{B}_x(x - x_0, t)\exp(ik_y y + ik_z z)$$

$$\mathbf{k}\cdot\mathbf{B}(x = x_0) = 0$$

$$\tilde{B}_x(x = x_0, t) \neq 0$$

$$\frac{dn}{dx} \neq 0,\ \frac{dT}{dx} \neq 0,\ \frac{dJ_z}{dx} \neq 0 \text{ for } x = x_0$$

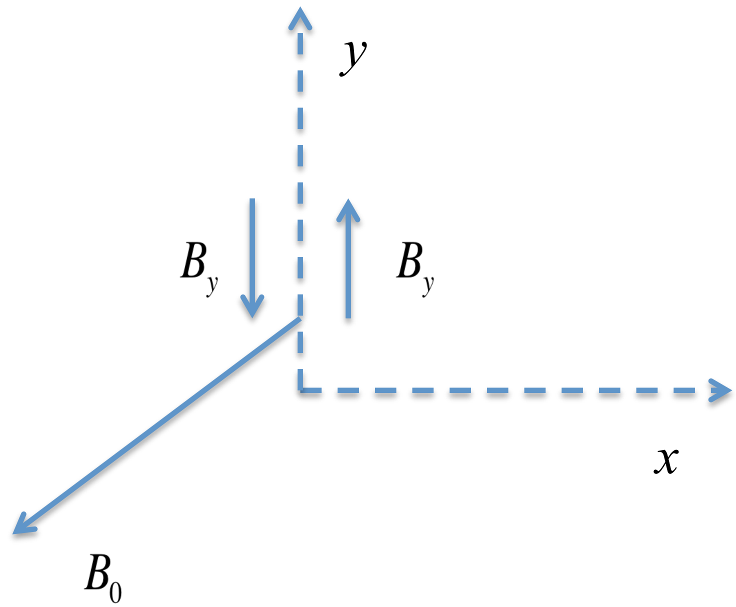

$J_z(x),\ n(x),\ T_i(x),\ T_e(x) \rightarrow$ even functions of x

Current Sheet: $\mathbf{B} \simeq B_0 \mathbf{e}_z + B_y(x)\mathbf{e}_y$

Temperature Singularities

electrons

$$\hat{T}_e = \tilde{T}(x)\exp\left(-\omega t + ik_y y + ik_z z\right)$$

$$\omega < \left(k_{||} V_{the}\right)\left(k_{||}\lambda_e\right)$$

$$\lambda_e = \frac{V_{the}}{\nu_e}$$

$$\boxed{i\left(\mathbf{k}\cdot\mathbf{B}\right)\hat{T}_e + \hat{B}_x \frac{dT_e}{dx}}$$

$$\mathbf{k}\cdot\mathbf{B} = \left(\mathbf{k}\cdot\mathbf{B}'\right)\left(x - x_0\right)$$

$$\hat{T}_e \propto \frac{\hat{B}_{x0}}{x - x_0}$$

nuclei

$$\left(k_{\parallel} V_{thi}\right)\left(k_{\parallel} \lambda_i\right) < \omega$$

in the “outer” (ideal MHD) region

$$\hat{T}_i \simeq -\hat{\xi}_x \frac{dT_i}{dx} \qquad \text{and} \qquad \hat{\xi}_x = \frac{d}{dt} \hat{u}_{ix}$$

while

$$\hat{B}_x \simeq i\left(\mathbf{k} \cdot \mathbf{B}\right)\hat{\xi}_x$$

In the inner region the singularity of $\hat{\xi}_x$ can be taken care of by the effects of finite resistivity. At the same time the relationship between $\hat{T}_i$ and $\hat{\xi}_x$ becomes

$$\hat{T}_i \simeq \hat{\xi}_x \frac{dT_i}{dx} + \frac{i}{\omega} D_{\perp i} \frac{\partial^2 \hat{T}_i}{\partial x^2}.$$

$\boxed{\text{Density Singularity}}$

$$\hat{n} \simeq -\frac{dn}{dx} \hat{\xi}_x$$

in the "outer" region where $\hat{\xi}_x \simeq -\frac{i}{\mathbf{k} \cdot \mathbf{B}} \hat{B}_x$

Note
Can these singularities be relevant to the generation of high energy particles by magnetic reconnection events?

Electron Inertia Scale Distance

1PeV= 10^{15} eV

$$m_e\left(\mathcal{E} \simeq 1\mathrm{PeV}\right) \simeq 10^6 m_i\left(\mathrm{rest}\right) \simeq 2\times 10^9 m_e\left(\mathrm{rest}\right)$$

$$\delta_{EI} \equiv \frac{c}{\omega_{pe}} \simeq 5.3\times 10^5 \frac{1}{n_e^{1/2}} \;\; \text{for } m_e\left(\mathrm{rest}\right) \;\; \mathrm{cm}$$

$$\delta_{EI}^{HE} = \frac{c}{\omega_{pe}^{HE}} \simeq 2.35\times 10^6 \left(\frac{10^{-2}}{n_e}\right)^{1/2} \mathrm{km}$$

"Breaking the frozen-in-law"

$$\boxed{E_{\parallel} = \eta_{\parallel} J_{\parallel} + \mathcal{L}_{\parallel} \frac{\partial J_{\parallel}}{\partial t}}$$

Inertial-Inductive Modes: A way out

Consider two classes of mode

- Ordinary reconnecting modes (of the kind that cannot be found within the Ideal-MHD approximation)

  Growth rate

$$\gamma \propto \delta_I^3 ,$$

  where

$$\delta_I \to \frac{c}{\omega_{pe}} \text{ (inertial)} \qquad \delta_I^2 \to S_L \text{ (inductive)},$$

  and

$$\delta_{rec} \sim \delta_I \frac{\delta_I}{r_J} \ll \delta_I$$

- Strongly Reconnecting modes (NMS, such as $m^0 = 1$ modes producing sawtooth oscillations)

$$\gamma \propto \delta_I$$

$$\delta_{rec} \sim \delta_I$$

NMS indicates “near Ideal-MHD marginal stability”.

Therefore, in order to explain the observation of fast reconnection events with realistic small-scale structures the excitation of Strongly Reconnecting modes can be a reasonable option.

Note that the most important class of reconnecting modes involve wavelengths and radial extensions of the order of the radius of the plasma column. Thus the coupling (represented by an inductivity) to fields produced by currents not directly associated with the modes themselves can be more easily envisioned than for short wavelength modes.

where

$$\eta_{\|} \equiv \frac{4\pi}{c^2} D_m, \qquad \mathcal{L}_{\|} \equiv \frac{4\pi}{c^2} S_L, \qquad E_{\|} \neq 0.$$

Therefore

$$E_{\|} = \frac{4\pi}{c^2}\left[D_m J_{\|} + S_L \frac{\partial J_{\|}}{\partial t} \right]$$

where

$$S_L \geq \frac{c^2}{\omega_{pe}^2}$$

$\eta_{\|} =$ longitudinal resistivity

$\mathcal{L}_{\|} =$ inductivity

$D_m =$ magnetic diffusion coefficients.

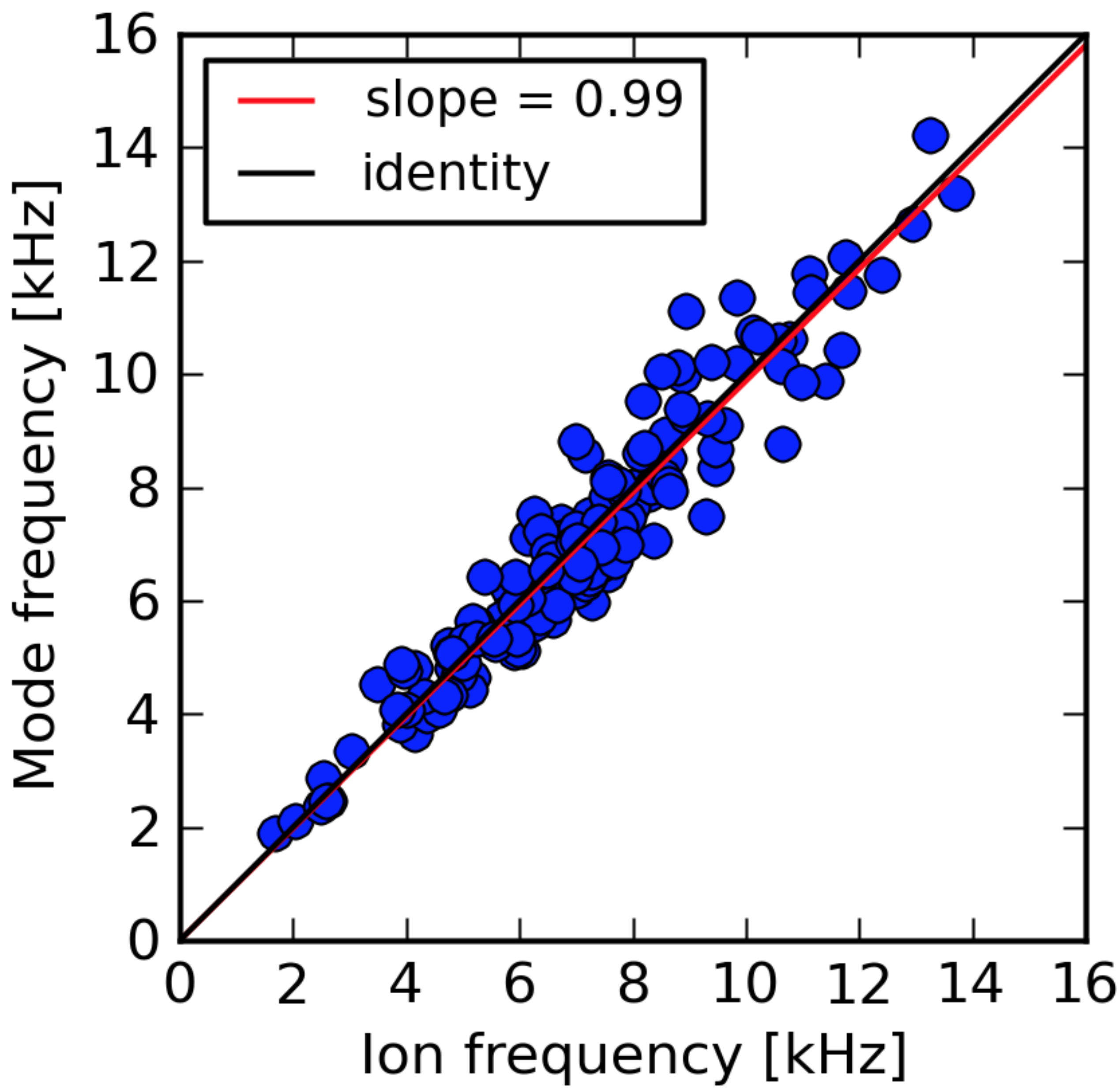

slope = 0.99
identity
Mode frequency [kHz]
Ion frequency [kHz]
0
2
4
6
8
10
12
14
16

"INERTIAL" INSTABILITIES IN PLASMAS *

B. COPPI
Division of Applied Physics, Stanford University, Stanford, California

Received 22 June 1964

The search for a physically acceptable auroral "dumping" instability [1], and the difficulty in explaining the features of an instability found experimentally [2,3] have led to consider the effects of electron inertia. In particular, a theory based on the asymptotic solution of moment equations which take simultaneously into account the influence of collisions [4], ion Larmor radius [5,6] and electron inertia has led to finding: a) A class of new "inertial" modes driven by the local gradient of the current flowing along the magnetic field. b) An inertial mode with growth rate of the same order of magnitude, but related to the profile of the equilibrium quantities far from the region where electron inertia is important. This factor makes topologically possible the transfer of potential energy stored in the magnetic field to plasma kinetic energy [7], as the constraint that the guiding centres move with the lines of force is released [8]. c) The known resistive tearing mode [4,5] driven by the same mechanism, which is stabilised for very low pressures by the electron inertia if local gradients of the current longitudinal to the magnetic field are negligible. d) The known resistive interchange modes, on which electron inertia superimposes only stable oscillations, when a gravitational field is present in the equilibrium.

We make use of the complete form of the "Ohm's law" as derived from the kinetic equations for ion and electrons [9]. For the terms expressing the effects of collisions and for the pressure tensor we use expressions obtained from the Fokker-Planck equation [10]. We shall use Gaussian units with $c = 1$ and a set of local coordinates, $\boldsymbol{e}_{\parallel} \equiv \boldsymbol{B}/B$, $\boldsymbol{e}_x$ and $\boldsymbol{e}_{\perp} \equiv \boldsymbol{e}_{\parallel} \times \boldsymbol{e}_x$, where $\boldsymbol{B}$ is the magnetic field. Derivatives with respect to x will be indicated by "prime".

As an equilibrium configuration, we consider a layer perpendicular to $\boldsymbol{e}_x$, of width R, where all quantities are only x-dependent and $\boldsymbol{B}\cdot\boldsymbol{e}_x = 0$. The equilibrium is defined over a time scale less than the mass diffusion time [6], and characterised by $-\boldsymbol{B}\cdot\boldsymbol{B}' = p'$, θ = constant, $p_e = p_i$ and $v_b = p_i'/(\Omega\rho)\boldsymbol{e}_{\perp}$, where p_i and p_e are ion and electron pressures, $p = p_i + p_e$, ρ the mass density, $\theta \equiv p_i/\rho$, Ω the ion gyro-frequency, and v_b an ion bulk velocity. From previous analyses [4-6] we expect ion Larmor radius, electron inertia and collisional effects to be important in a region of width ϵR around the surface $x = x_0$ where $\boldsymbol{k}\cdot\boldsymbol{B} = 0$.

A. Let $s\xi(\boldsymbol{r}, t) = s\xi(x) \exp(st + \mathrm{i}\boldsymbol{k}\cdot\boldsymbol{r})$, where $\boldsymbol{k}\cdot\boldsymbol{e}_x = 0$ and $s \equiv \gamma + \mathrm{i}\omega$, represent a perturbation of the ion velocity around its equilibrium value. Then assuming $p'R/p = \mathrm{O}(1)$ and $\beta \ll \epsilon \ll 1$, so that $\boldsymbol{B}\cdot\boldsymbol{B}'R/B^2 = \mathrm{O}(\beta)$, the lowest order set of equations, corresponding to the fastest mode localised in ϵR, is

$$s^2 \rho \xi_x'' = \mathrm{i}(\boldsymbol{k}\cdot\boldsymbol{B})\tilde{B}_x'' , \tag{1}$$

$$B\tilde{B}_{\parallel} = -\tilde{p} = p'\xi_x(1 + \mathrm{i}kv_b/s)^{-1} , \tag{2}$$

* Work supported by the Air Force Scientific Research on Contract AF 49(638)-1321.

PHYSICS OF PLASMAS 21, 022510 (2014)

Compressible magnetohydrodynamic sawtooth crash

Linda E. Sugiyama
Laboratory for Nuclear Science, Massachusetts Institute of Technology, Cambridge, Massachusetts 02139-4307, USA

(Received 15 August 2013; accepted 30 January 2014; published online 24 February 2014)

In a toroidal magnetically confined plasma at low resistivity, compressible magnetohydrodynamic (MHD) predicts that an $m=1/n=1$ sawtooth has a fast, explosive crash phase with abrupt onset, rate nearly independent of resistivity, and localized temperature redistribution similar to experimental observations. Large scale numerical simulations show that the 1/1 MHD internal kink grows exponentially at a resistive rate until a critical amplitude, when the plasma motion accelerates rapidly, culminating in fast loss of the temperature and magnetic structure inside $q<1$, with somewhat slower density redistribution. Nonlinearly, for small effective growth rate the perpendicular momentum rate of change remains small compared to its individual terms ∇p and $\mathbf{J}\times\mathbf{B}$ until the fast crash, so that the compressible growth rate is determined by higher order terms in a large aspect ratio expansion, as in the linear eigenmode. Reduced MHD fails completely to describe the toroidal mode; no Sweet-Parker-like reconnection layer develops. Important differences result from toroidal mode coupling effects. A set of large aspect ratio compressible MHD equations shows that the large aspect ratio expansion also breaks down in typical tokamaks with $r_{q=1}/R_o \simeq 1/10$ and $a/R_o \simeq 1/3$. In the large aspect ratio limit, failure extends down to much smaller inverse aspect ratio, at growth rate scalings $\gamma = O(\epsilon^2)$. Higher order aspect ratio terms, including $\tilde{B}_\phi$, become important. Nonlinearly, higher toroidal harmonics develop faster and to a greater degree than for large aspect ratio and help to accelerate the fast crash. The perpendicular momentum property applies to other transverse MHD instabilities, including $m \geq 2$ magnetic islands and the plasma edge.
[http://dx.doi.org/10.1063/1.4865571]

I. INTRODUCTION

Periodic sawtooth crashes of the central temperature in magnetically confined fusion plasmas have been observed since the first tokamaks. A helical $m=1/n=1$ poloidal/toroidal structure was first identified in 1974.[1] Kadomtsev's nonlinear model for the crash,[2] based on helical flux conservation, appeared to be confirmed by experiments[3] and numerical simulations,[4] although it has since been called into question. The sawtooth crash is still incompletely understood and experimental investigation continues.[5,6]

Sawteeth are important for fusion burning because the crash amplitude increases with central heating. Since fusion reactivity increases with ion temperature, large sawteeth could significantly degrade burning conditions. Projected fusion burning regimes in the ITER experiment[7] have a large $q=1$ radius $r_1 \simeq a/2$, due to the high plasma current and low values of edge safety factor $q_{95} < 3.5$. High central temperatures $T_o \sim 20$ keV generated by fusion give the potential for larger sawteeth than in existing plasmas.

The 1/1 mode has been extensively analyzed in a torus and represents a paradigm for the analytical treatment of toroidal instabilities. It involves a helical displacement of the entire central core of the plasma inside the magnetic surface with $q=m/n=1$. Two main types of MHD instability with $n=1$ can be driven by the equilibrium pressure gradient over $q<1$ when the central $q_o<1$—the internal kink in ideal MHD[8–10] and resistive[11–15] versions, or at low magnetic shear with $q \lesssim 1$, the quasi-interchange[16–18] or current-driven[18] modes. For the incompressible ideal MHD internal kink,[10] large aspect ratio expansion, $R/a \gg 1$, shows that higher order $m \neq 1$ poloidal harmonics driven by toroidal mode coupling introduce a minimum value of poloidal beta for toroidal instability, compared to zero beta in a cylinder. Complete large aspect ratio solutions exist for the incompressible[19] and (nominally) the compressible[20] mode.

Experimentally, sawteeth exhibit great variability. Nevertheless, in high temperature fusion plasmas they share several common features. The crash time is very short compared to the sawtooth period and also on absolute scales, on the order of a couple hundred shear Alfvén times, or 20 μs in small plasmas such as Alcator C-Mod or MAST to 100–200 μs in larger plasmas such as DIII-D and JET. The fast temperature redistribution during the crash[21,22] does not match the Kadomtsev model.[2]

The rapidity of the crash poses a serious theoretical problem. The exponential growth rate of the linear 1/1 eigenmode at a fractional power of the resistivity, $\gamma \sim \eta^{1/3}$ or $\eta^{3/5}$, predicts far too slow a crash at the low values of resistivity in fusion plasmas. Early nonlinear studies with a 2D helical incompressible MHD model demonstrated[23] modified Sweet-Parker[24] reconnection at small resistivity and reconnection rates compatible with observations on early large tokamaks. Nonlinear theories[25–27] made major simplifications, effectively dropping the higher order aspect ratio terms and $m \neq 1$ harmonics, despite their importance in the linear

RESEARCH ARTICLES

BLACK HOLE PHYSICS

Black hole lightning due to particle acceleration at subhorizon scales

J. Aleksić,[1] S. Ansoldi,[2] L. A. Antonelli,[3] P. Antoranz,[4] A. Babic,[5] P. Bangale,[6] J. A. Barrio,[7] J. Becerra González,[8*] W. Bednarek,[9] E. Bernardini,[10] B. Biasuzzi,[2] A. Biland,[11] O. Blanch,[1] S. Bonnefoy,[7] G. Bonnoli,[3] F. Borracci,[6] T. Bretz,[12†] E. Carmona,[13] A. Carosi,[3] P. Colin,[6] E. Colombo,[8] J. L. Contreras,[7] J. Cortina,[1] S. Covino,[3] P. Da Vela,[4] F. Dazzi,[6] A. De Angelis,[2] G. De Caneva,[10] B. De Lotto,[2] E. de Oña Wilhelmi,[14] C. Delgado Mendez,[13] D. Dominis Prester,[5] D. Dorner,[12] M. Doro,[15] S. Einecke,[16] D. Eisenacher,[12**] D. Elsaesser,[12] M. V. Fonseca,[7] L. Font,[17] K. Frantzen,[16] C. Fruck,[6] D. Galindo,[18] R. J. García López,[8] M. Garczarczyk,[10] D. Garrido Terrats,[17] M. Gaug,[17] N. Godinović,[5] A. González Muñoz,[1] S. R. Gozzini,[10] D. Hadasch,[14‡] Y. Hanabata,[19] M. Hayashida,[19] J. Herrera,[8] D. Hildebrand,[11] J. Hose,[6] D. Hrupec,[5] W. Idec,[9] V. Kadenius,[20] H. Kellermann,[6] K. Kodani,[19] Y. Konno,[19] J. Krause,[6] H. Kubo,[19] J. Kushida,[19] A. La Barbera,[3] D. Lelas,[5] N. Lewandowska,[12] E. Lindfors,[20§] S. Lombardi,[3] F. Longo,[2] M. López,[7] R. López-Coto,[1] A. López-Oramas,[1] E. Lorenz,[#] I. Lozano,[7] M. Makariev,[21] K. Mallot,[10] G. Maneva,[21] N. Mankuzhiyil,[2||] K. Mannheim,[12**] L. Maraschi,[3] B. Marcote,[18] M. Mariotti,[15] M. Martínez,[1] D. Mazin,[6] U. Menzel,[6] J. M. Miranda,[4] R. Mirzoyan,[6] A. Moralejo,[1] P. Munar-Adrover,[18] D. Nakajima,[19] A. Niedzwiecki,[9] K. Nilsson,[20§] K. Nishijima,[19] K. Noda,[6] R. Orito,[19] A. Overkemping,[16] S. Paiano,[15] M. Palatiello,[2] D. Paneque,[6] R. Paoletti,[4] J. M. Paredes,[18] X. Paredes-Fortuny,[18] M. Persic,[2] J. Poutanen,[20] P. G. Prada Moroni,[22] E. Prandini,[11] I. Puljak,[5] R. Reinthal,[20] W. Rhode,[16] M. Ribó,[18] J. Rico,[1] J. Rodriguez Garcia,[6] S. Rügamer,[12] T. Saito,[19] K. Saito,[19] K. Satalecka,[7] V. Scalzotto,[15] V. Scapin,[7] C. Schultz,[15] T. Schweizer,[6] S. N. Shore,[22] A. Sillanpää,[20] J. Sitarek,[1**] I. Snidaric,[5] D. Sobczynska,[9] F. Spanier,[12] V. Stamatescu,[1¶] A. Stamerra,[3] T. Steinbring,[12] J. Storz,[12] M. Strzys,[6] L. Takalo,[20] H. Takami,[19] F. Tavecchio,[3] P. Temnikov,[21] T. Terzić,[5] D. Tescaro,[8] M. Teshima,[6,19] J. Thaele,[16] O. Tibolla,[12] D. F. Torres,[23] T. Toyama,[6] A. Treves,[24] M. Uellenbeck,[16] P. Vogler,[11] R. Zanin,[18] M. Kadler,[12] R. Schulz,[12,25] E. Ros,[26,27,28] U. Bach,[26] F. Krauß,[12,25] J. Wilms[25]

Supermassive black holes with masses of millions to billions of solar masses are commonly found in the centers of galaxies. Astronomers seek to image jet formation using radio interferometry but still suffer from insufficient angular resolution. An alternative method to resolve small structures is to measure the time variability of their emission. Here we report on gamma-ray observations of the radio galaxy IC 310 obtained with the MAGIC (Major Atmospheric Gamma-ray Imaging Cherenkov) telescopes, revealing variability with doubling time scales faster than 4.8 min. Causality constrains the size of the emission region to be smaller than 20% of the gravitational radius of its central black hole. We suggest that the emission is associated with pulsar-like particle acceleration by the electric field across a magnetospheric gap at the base of the radio jet.

More than three decades ago, it was proposed that the radio emission of extragalactic jets results from a relativistically moving plasma consisting of magnetic fields and accelerated particles following a power-law energy distribution (*1*). One of the major assets of the model is that it can explain the nonthermal emission of extragalactic jets across the entire electromagnetic spectrum, from radio waves up to gamma rays. The emission can be understood as synchrotron radiation and inverse Compton scattering (*2*, *3*) due to particles accelerated at shock waves in the jets. The gamma rays can reach very high energies measured in giga–electron volts (1 GeV= 10^9 eV, corresponding roughly to the rest mass energy equivalent of the proton) and tera–electron volts (1 TeV = 10^{12} eV). According to the Blandford-Znajek mechanism, the jets are powered by extracting rotational energy from the black holes, which have acquired angular momentum through the accretion of surrounding gas and black hole mergers (*4*), although so far astrophysical evidence for the role of black hole spin is still lacking (*5*). For a maximally rotating supermassive black hole of mass $M = 10^8\, m_8\, M_\odot$, where $M_\odot$ denotes one solar mass, the size of the jet formation region should be of the order of its gravitational radius, $r_g = G_N M/c^2 \sim 1.5 \times 10^{11} m_8$ m (G_N, gravitational constant; c^2, speed of light) and twice this value for a nonrotating Schwarzschild black hole. Astronomical telescopes do not yet provide the angular resolution needed to image structures on this scale. The highest-resolution images of jets obtained with very long baseline radio interferometry show radio-emitting knots traveling down the jets (*6*). Approaching the black hole, the spectra cut off at increasingly higher frequencies due to synchrotron self-absorption. Observations at very high frequencies where the core becomes transparent are needed to zoom into the region where the jets are emerging from. The record holder is a very long baseline radio interferometry observation of the jet of the nearby radio galaxy M87 at a frequency of 230 GHz, resolving a source with a size of 11.0 ± 0.8 gravitational radii (*7*).

The event horizon light-crossing time

Although direct imaging of the jet formation region has to await better angular resolution, indirect information about its size can be inferred

[1]Institut de Física d'Altes Energies, Campus UAB, E-08193 Bellaterra, Spain. [2]Università di Udine and Istituto Nazionale di Fisica Nucleare (INFN) Trieste, I-33100 Udine, Italy, and Istituto Nazionale di Astrofisica (INAF)-Trieste, I-34127 Trieste, Italy. [3]INAF National Institute for Astrophysics, I-00136 Rome, Italy. [4]Università di Siena and INFN Pisa, I-53100 Siena, Italy. [5]Croatian MAGIC Consortium, Rudjer Boskovic Institute, University of Rijeka and University of Split, HR-10000 Zagreb, Croatia. [6]Max-Planck-Institut für Physik, D-80805 München, Germany. [7]Universidad Complutense, E-28040 Madrid, Spain. [8]Instituto de Astrofísica de Canarias, E-38200 La Laguna, Tenerife, Spain. [9]University of Łódź, PL-90236 Lodz, Poland. [10]Deutsches Elektronen-Synchrotron, D-15738 Zeuthen, Germany. [11]ETH Zurich, CH-8093 Zurich, Switzerland. [12]Universität Würzburg, D-97074 Würzburg, Germany. [13]Centro de Investigaciones Energéticas, Medioambientales y Tecnológicas, E-28040 Madrid, Spain. [14]Institute of Space Sciences, E-08193 Barcelona, Spain. [15]Università di Padova and INFN, I-35131 Padova, Italy. [16]Technische Universität Dortmund, D-44221 Dortmund, Germany. [17]Unitat de Física de les Radiacions, Departament de Física, and Centro de Estudios e Investigación Espaciales-Institut d'Estudis Espacials de Catalunya, Universitat Autònoma de Barcelona, E-08193 Bellaterra, Spain. [18]Universitat de Barcelona, Institut de Ciències del Cosmos, Institut d'Estudis Espacials de Catalunya-Universitat de Barcelona, E-08028 Barcelona, Spain. [19]Japanese MAGIC Consortium, Division of Physics and Astronomy, Kyoto University, Japan. [20]Finnish MAGIC Consortium, Tuorla Observatory, University of Turku and Department of Physics, University of Oulu, Finland. [21]Institute for Nuclear Research and Nuclear Energy, BG-1784 Sofia, Bulgaria. [22]Università di Pisa and INFN Pisa, I-56126 Pisa, Italy. [23]ICREA and Institute of Space Sciences, E-08193 Barcelona, Spain. [24]Università dell'Insubria and INFN Milano Bicocca, Como, I-22100 Como, Italy. [25]Dr. Remeis-Sternwarte Bamberg, Astronomisches Institut der Universität Erlangen-Nürnberg, ECAP, D-96049 Bamberg, Germany. [26]Max-Planck-Institut für Radioastronomie, D-53121 Bonn, Germany. [27]Observatori Astronòmic, Universitat de València, E-46980 Paterna, València, Spain. [28]Departament d'Astronomia i Astrofísica, Universitat de València, E-46100 Burjassot, València, Spain.
*Present address: NASA Goddard Space Flight Center, Greenbelt, MD 20771, USA, and Department of Physics and Department of Astronomy, University of Maryland, College Park, MD 20742, USA. †Present address: Ecole Polytechnique Fédérale de Lausanne (EPFL), Lausanne, Switzerland. ‡Present address: Institut für Astro- und Teilchenphysik, Leopold-Franzens-Universität Innsbruck, A-6020 Innsbruck, Austria. §Present address: Finnish Centre for Astronomy with ESO (FINCA), Turku, Finland. ||Present address: Astrophysics Science Division, Bhabha Atomic Research Centre, Mumbai 400085, India. ¶Present address: School of Chemistry and Physics, University of Adelaide, Adelaide 5005, Australia. #Deceased. **Corresponding author. E-mail: deisenacher@astro.uni-wuerzburg.de (D.E.); jsitarek@ifae.es (J.S.), mannheim@astro.uni-wuerzburg.de (K.M.)**

value of the Doppler factor (section S1.2). The probability of such an alignment seems to be rather low. Moreover, the observed radio jet does not show any signs of a perturbation of its flow direction on the parsec and kiloparsec scales. Because perturbations of the flow direction of the inner jet would later propagate to larger scales, major bends apparently never occurred in the past.

In summary, trying to interpret the data in the frame of the shock-in-jet model meets difficulties. Considering the role of time dilation renders a solution of this problem impossible for any value of Γ_j. Therefore, we conclude that the observations indicate a subhorizon-scale emission region of a different nature.

Possible origins of subhorizon-scale variability

Substructures smaller than the event horizon scale emitting highly anisotropic radiation (to avoid pair absorption) seem to be responsible for the minute-scale flux variations. The possible explanations fall into three categories: (i) mini-jet structures within the jets (*33*); (ii) jet-cloud interactions, where the clouds may originate from stellar winds (*34*–*36*); and (iii) magnetospheric models (*37*–*41*), similar to those known from pulsar theory.

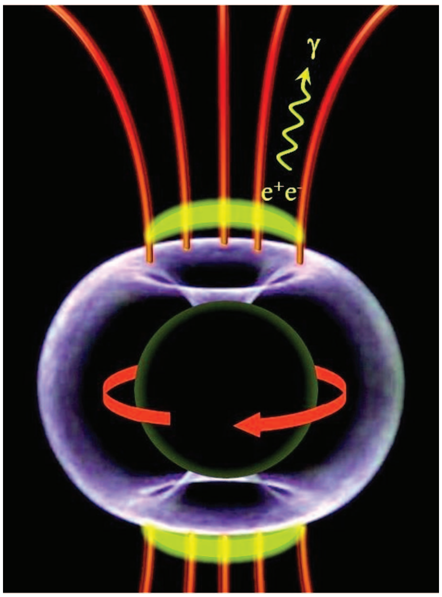

Fig. 5. Scenario for the magnetospheric origin of the gamma rays: A maximally rotating black hole with event horizon r_g (black sphere) accretes plasma from the center of galaxy IC 310. In the apple-shaped ergosphere (blue) extending to $2r_g$ in the equatorial plane, Poynting flux is generated by the frame-dragging effect. The rotation of the black hole induces a charge-separated magnetosphere (red) with polar vacuum gap regions (yellow). In the gaps, the electric field of the magnetosphere has a component parallel to the magnetic field that is accelerating particles to ultrarelativistic energies. Inverse Compton scattering and copious pair production due to interactions with low-energy thermal photons from the plasma accreted by the black hole lead to the observed gamma rays.

According to the mini-jet model (i), plasmoids resulting from magnetic reconnection traveling down the jet with a relativistic speed are responsible for the minute-scale flux variations observed in blazars. The model could help to mitigate the constraints on the bulk Lorentz factor by introducing a larger effective bulk Lorentz factor for the plasmoids. The mechanism also predicts reconnection events from regions outside of the beaming cone $\sim\Gamma_j^{-1}$ that could explain the day-scale flares from the radio galaxy M87 invoking external radiation fields as a target for inverse Compton scattering (*33*). However, the off-axis mini-jet luminosity depends on $(\Gamma_j\theta)^{-8}$, and the jet power required for IC 310 is two orders of magnitude higher than the one estimated from radio observations (section S3.2). Thus, this model is challenged by the observed high luminosity in IC 310 during the flares.

Substructures smaller than the jet radius may also be introduced by considering interactions between clouds and the jet (ii). The original shock-in-jet model (*1*) considered this to be the main source of mass entrainment and predicted variability from the process. Recently, more elaborate work on the model has had some success in explaining the variability of M87 by proton-proton collisions due to the bombardment of clouds boiled off of red giants with protons in the jet (*36*). However, the model is linked to the cloud crossing time of the jet and the proton-proton cooling time, both of which far exceed the event horizon scale. Faster variability could be observed if the cloud gets destroyed, but a strong beaming effect would then be needed to explain the observed luminosities. In another variant, drift acceleration of particles along the trailing shock behind the stellar wind of a star interacting with the jet is considered. This might lead to an extremely anisotropic emission pattern. As mass-loosing stars sweep across the jet, passing magnetic field lines pointing to the observer, the postulated accelerated particle beams in their trails become visible for a short time. For IC 310, the emission would have to be confined to within an angle of $\alpha\sim10^{-5}$ rad to explain the observed variability time scale, requiring a very stable direction of the accelerated particle beams, at a large angle to the jet main thrust. Because two-fluid particle beams are prone to numerous plasma instabilities, the scenario relies on unphysical assumptions.

In magnetospheric models (iii), particle acceleration is assumed to be due to electric fields parallel to the magnetic fields. This mechanism is known to operate in the particle-starved magnetospheres of pulsars, but it could also operate in the magnetospheres anchored to the ergospheres of accreting black holes (Fig. 5). Electric fields can exist in vacuum gaps when the density of charge carriers is too low to warrant their shortcut. The critical charge density for the vacuum gaps is the so-called Goldreich-Julian charge density. Electron-positron pairs in excess of the Goldreich-Julian charge density can be produced thermally by photon-photon collisions in a hot accretion torus or corona surrounding the black hole. It has also been suggested that particles can be injected by the reconnection of twisted magnetic loops in the accretion flow (*39*). A depletion of charges from thermal pair production is expected to happen when the accretion rate becomes very low. In this late phase of their accretion history, supermassive black holes are expected to have spun up to maximal rotation. Black holes can sustain a Poynting flux jet by virtue of the Blandford-Znajek mechanism (*4*). Jet collimation takes place rather far away from the black hole at the scale of the light cylinder beyond $\sim10r_g$. Gaps could be located at various angles, with the jet axis corresponding to the polar and outer gaps in pulsar magnetospheres leading to fan beams at rather large angles with the jet axis. The gap emission must be highly variable, because gap height and seed particle content depend sensitively on plasma turbulence and accretion rate. For an accretion rate of $\dot{m}\sim10^{-4}$ (in units of the Eddington accretion rate) and maximal black hole rotation, the gap height in IC 310 is expected to be $h\sim0.2\,r_g$ (*40*), which is in line with the observations. Depending on the electron temperature and geometry of the radiatively inefficient accretion flow, its thermal cyclotron luminosity can be low enough to warrant the absence of pair creation attenuation in the spectrum of gamma rays. In this picture, the intermittent variability witnessed in IC 310 is due to a runaway effect. As particles accelerate to ultrahigh energies, electromagnetic cascades develop, multiplying the number of charge carriers until their current shortcuts the gap. The excess particles are then swept away with the jet flow, until the gap reappears.

Radio galaxies and blazars with very low accretion rates allow us to obtain a glimpse of the jet formation process near supermassive black holes. The subhorizon variability in combination with the results from direct imaging campaigns invite us to explore analogies with pulsars, where particle acceleration takes place in two stages. In the first stage, particle acceleration occurs in the gaps of a charge-separated magnetosphere anchored in the ergosphere of a rotating black hole, and in a second stage, particle acceleration occurs at shock waves in the force-free wind beyond the outer light cylinder.

REFERENCES AND NOTES

1. R. D. Blandford, A. Königl, *Astrophys. J.* **232**, 34 (1979).
2. L. Maraschi, G. Ghisellini, A. Celotti, *Astrophys. J.* **397**, L5 (1992).
3. C. D. Dermer, R. Schlickeiser, *Astrophys. J.* **416**, 458 (1993).
4. R. D. Blandford, R. L. Znajek, *Mon. Not. R. Astron. Soc.* **179**, 433–456 (1977).
5. S. van Velzen, H. Falcke, *Astron. Astrophys.* **557**, L7 (2013).
6. A. P. Marscher, W. K. Gear, *Astrophys. J.* **298**, 114 (1985).
7. S. S. Doeleman *et al.*, *Science* **338**, 355–358 (2012).
8. I. Vovk, A. Neronov, *Astrophys. J.* **767**, 103 (2013).
9. J. Albert *et al.*, *Astrophys. J.* **685**, L23–L26 (2008).
10. A. Abramowski *et al.*, *Astrophys. J.* **746**, 151 (2012).
11. K. Gebhardt, J. Thomas, *Astrophys. J.* **700**, 1690–1701 (2009).
12. V. A. Acciari *et al.*, *Science* **325**, 444–448 (2009).
13. J. Albert *et al.*, *Astrophys. J.* **669**, 862–883 (2007).
14. F. Aharonian *et al.*, *Astrophys. J.* **664**, L71–L74 (2007).
15. M. C. Begelman, A. C. Fabian, M. J. Rees, *Mon. Not. R. Astron. Soc.* **384**, L19–L23 (2008).
16. In special relativity, the Lorentz and Doppler factors are defined as $\Gamma_j = (1-\beta^2)^{-1/2}$ and

Mesoscopic Reconnection

- Involves a reconnecting layer which remains significant even when the macroscopic scale distances characterizing the problem become very large.

- This is the case for the so-called internal kink mode ($m^0=1$) that involves reconnection and can develop in a cylindrical or toroidal geometry. But this is not the case for the so-called tearing modes.

- The mesoscopic modes we consider involve the effects of the plasma density and temperature gradients and depend on the relevant finite inductivity that make the reconnection layer larger than the ion gyro-radius. Unlike tearing modes these modes are not driven by the plasma current density gradient and are localized with in the reconnection layer.

- When considering a plane symmetric plasma current sheet we may classify the resulting process as a "lateral reconnection" taking place away from the central plane.

Resistive internal kink modes

B. Coppi[1, 2] R. Galvão[1, 2] R. Pellat[1, 3] M. Rosenbluth,[4] and P. Rutherford[5]

Fiz. Plazmy 2, 961–966 (November-December 1976)

For realistic parameters of magnetically confirmed plasmas the growth rates on internal kink modes, resulting from the effects of finite electrical resistivity, can be considerably larger than those evaluated from the idealized MHD theory. In addition, magnetic field lines can reconnect and produce configurations with magnetic islands.

PACS numbers: 52.35.En, 52.52.Gj

We consider, for simplicity, a magnetically confined, current carrying cylindrical plasma column of length $2\pi R$, in which $B_Z(r)$ and $B_\theta(r)$ are the axial and azimuthal components of the magnetic field. The so-called internal kink mode is characterized by an azimuthal wave number $m = 1$ and by leaving the plasma boundary unperturbed. This mode can be excited whenever there is a region inside the plasma column where the value of the quantity $q(r) \equiv rB_Z(r)/[R\,B_\theta(r)]$ falls below unity within the region, and increases monotonically outside it to a value above unity at the plasma boundary.[1]

The experimental work reported in Ref. 2 has confirmed that $|m| = 1$ oscillations do occur inside a toroidal plasma column when the value of q(r) falls below unity at the magnetic axis, and that the radial mode structure is in reasonable agreement with the theoretical predictions. However, the ideal MHD treatment of this mode including a nonlinear analysis of it[3] is not sufficient to explain other important features of the observed oscillations such as their frequency and the values of their amplitudes.

We recall that the ideal MHD theoretical growth rate of the internal kink mode, γ_{MHD}, is considerably smaller than that of the "free-boundary" kink mode, as $\gamma_{MHD} \sim (r_0/R)^2/\tau_H$, where $\tau_H \equiv r_0/v_{A\theta}$, $v_{A\theta}^2 \equiv [B_\theta^2/(4\pi\rho)] \times (q' r_0/q)^2$, $r = r_0$ is the surface at which $q(r) = 1$, ρ is the mass density, $q' = dq/dr$, and $v_{A\theta}$ is evaluated at r_0. In considering the effects of finite electrical resistivity η we define a magnetic diffusion coefficient $D_m \equiv \eta c^2/4\pi$, a resistive diffusion time $\tau_R \equiv r_0^2/D_m$, and a parameter $\varepsilon \equiv \tau_H/\tau_R$ that is taken to be small. Then on the basis of the general results obtained in Ref. 4, we expect the growth rate of this mode to be of order $\gamma \sim \varepsilon^{1/3}/\tau_H$ whenever $\gamma_{MHD}\tau_H \lesssim \varepsilon^{1/3}$, a condition that is frequently realized in current experiments.

In addition the effects of resistivity lead to a different topology of the perturbed magnetic field that is consistent with the formation of magnetic islands. The linear resistive treatment of this mode is still not sufficient to account for the frequencies and amplitudes of the observed oscillations but is the necessary first step in this direction and in order to establish the relevance of the $m = 1$ mode[3] to the onset of the so-called disruptive instability.[5]

We refer to the following linearized equations for small perturbations of the considered cylindrical plasma column:

$$\rho\frac{\partial}{\partial t}\mathbf{v}_1=-\nabla p_1+\frac{1}{c}\mathbf{J}_1\times\mathbf{B}+\frac{1}{c}\mathbf{J}\times\mathbf{B}_1,$$

$$\frac{\partial}{\partial t}\mathbf{B}_1=\nabla\times(\mathbf{v}_1\times\mathbf{B})-\eta c\nabla\times\mathbf{J}_1,$$

where the subscript 1 indicates perturbed quantities, $\mathbf{J}_1 = (\nabla\times\mathbf{B}_1)c/(4\pi)$, $\mathbf{J} = (\nabla\times\mathbf{B})c/4\pi$, and the resistivity η has been considered as constant for simplicity. In particular, we look for normal mode solutions of the form $\mathbf{v}_1(t, r, \theta, z) = \mathbf{v}_1(r)\exp[\gamma t + i(m\theta + kz)]$, where $k \equiv 1/R$; R is the major radius of the toroidal configuration that is simulated. Then, following a procedure outlined in Ref. 6, in order to reduce the stability problem to a couple of equations in the radial components v_{1r} and B_{1r}, we apply the operator $\mathbf{B}\cdot\nabla\times$ to the first of the equations given above and take the radial component of the second. We recall that $(kr)^2 = (r/R)^2 \ll m^2$ and obtain

$$4\pi\gamma\left[\frac{1}{r}\frac{d}{dr}\rho r^3\frac{dv_{1r}}{dr}-\rho(m^2-1)v_{1r}\right]=irF\left[\frac{1}{r}\frac{d}{dr}r\frac{d}{dr}(rB_{1r})-\frac{1}{Fr^2}\left\{m^2G+\frac{d}{dr}r\frac{d}{dr}(rF)\right\}(rB_{1r})\right], \tag{1}$$

$$\gamma B_{1r}=iFv_{1r}+\frac{\eta c^2}{4\pi}\left[\frac{1}{r^3}\frac{d}{dr}\left(r^3\frac{dB_{1r}}{dr}\right)-\frac{m^2-1}{r^2}B_{1r}\right]. \tag{2}$$

The quantities F and G are defined as

$$F\equiv mB_\theta/r+kB_z, \tag{3}$$

$$G\equiv F\frac{m^2+k^2r^2-1}{m^2}+2\frac{k^2r^2}{m^4}\left(kB_z-\frac{m}{r}B_\theta\right). \tag{3'}$$

In the limit of zero resistivity we obtain simply[7]

$$\frac{d}{dr}\left[r^3(4\pi\rho\gamma^2+F^2)\frac{d\xi}{dr}\right]-g\xi=0 \tag{4}$$

for $m = -1$ modes, where we have defined $v_{1r} = \gamma\xi$, $g \equiv FGr$,

Electron Thermal Energy Balance Equation

$$\frac{D^e_{\perp th}}{D^e_{\| th}} \frac{d^2 \tilde{T}_e}{dx^2} - k_\|^2 \tilde{T}_e \simeq -ik_\| \frac{\tilde{B}_x}{B} \frac{dT_e}{dx} \tag{1}$$

where $Bk_\| \simeq \mathbf{k} \cdot \mathbf{B}'(x - x_0) \simeq k_y B'_y (x - x_0)$.

Introducing the variables

$$\bar{x} \equiv \frac{x - x_0}{\delta_I}, \qquad \tilde{b} \equiv -k_y \frac{\tilde{B}_x}{B'_y}, \qquad \tilde{\tau} \equiv -\frac{\tilde{T}_e}{T'_e} k_y^2 \delta_I,$$

where $|k_y \delta_I| \ll 1$, Eq. (1) becomes

$$\left(\frac{\delta_T}{\delta_I}\right)^4 \frac{d^2 \tilde{\tau}}{d\bar{x}^2} - \bar{x}^2 \tilde{\tau} \simeq -i\tilde{b}\bar{x}, \tag{2}$$

where

$$\delta_T^4 \equiv \frac{D^e_{\perp th}}{D^e_{\| th}} \left(\frac{B}{B'_y k_y} \right)^2 . \tag{3}$$

It is evident that for, $\bar{x} \sim 1$ and $\tilde{\tau} \sim \tilde{b}$,

$$\left| \frac{\tilde{T}_e}{T'_e} \right| \sim \left| \frac{\tilde{B}_x}{B'_y} \frac{1}{\left(k_y \delta_I \right)} \right| \gg \left| \frac{\tilde{B}_x}{B'_y} \right| \tag{4}$$

and we may argue that **relatively large electron fluctuations** can be associated with significant reconnection fields.

The Fourier transform of Eq. (2) can be written as

$$\frac{d^2}{d\bar{k}^2}\tilde{\tau} - \Delta_T^4 \bar{k}^2 \tilde{\tau} \frac{d}{d\bar{k}} \tilde{b}, \tag{5}$$

where $\Delta_T \equiv \delta_T / \delta_I$, $\bar{k}^2 \equiv k_x^2 \delta_I^2$ and δ_I is the width of the (inductive) layer over which the mode is localized.

This is to be coupled to the following equation derived from the longitudinal electron momentum conservation equation

$$\left[\omega - \omega_{*e} - \omega_{*T} + \left(\omega + i\bar{D}_m\right)\bar{k}^2\right]\tilde{b} + \omega_{H*}^2 \frac{d}{d\bar{k}} \left\{\frac{1}{\omega + i\bar{D}_n \bar{k}} x \left[\frac{\delta_I^2}{\rho_s^2} \frac{\omega - \omega_{*e}}{\bar{k}^2\left(\omega - \omega_{di}\right)} + 1\right] \frac{d}{d\bar{k}}\left(\bar{k}^2 \tilde{b}\right)\right\} \simeq -\omega_{*T} \frac{d\tilde{\tau}}{d\bar{k}}, \tag{6}$$

where $\bar{D}_m \equiv D_m / \delta_I^2$, $\bar{D}_n \equiv D_n / \delta_I^2$, D_m is the magnetic (resistive diffusion

coefficient) and D_n the particle diffusion coefficient.
Note that, for $\Delta_T = 0$, Eq. (6) reduces to a 2nd order equation that does not contain ω_{*T}.

Relevant quadratic form, used to evaluate the mode real frequency, for $\omega \simeq \omega_{*e}$,

$$\begin{aligned}
&\Lambda\left\langle \frac{\tilde{b}^2}{\ell^2} + \left(\frac{d\tilde{b}}{d\ell}\right)^2 \right\rangle \simeq \eta_* \left\langle \left(\frac{d\tilde{\tau}}{d\ell}\right)^2 + \alpha_*\left(\ell\tilde{\tau}\right)^2 - \tilde{\tau}^2 \right\rangle \\
&+\left\langle \left(\ell\tilde{b}\right)^2 + \tilde{b}^2 - \left(\ell\frac{d\tilde{b}}{d\ell}\right)^2 \right\rangle
\end{aligned} \tag{7}$$

where $\ell \propto \overline{k}$, $\alpha_* \propto \Delta_T^4$, $\eta_* \propto \dfrac{d\ln T_e}{d\ln n}$ and $\Lambda \equiv \omega/\omega_{*e} - 1$.

Other Definitions

Perturbed B-field

$$\hat{B}_x = \tilde{B}_x(x)\exp\left(-i\omega t + ik_y y + ik_z z\right).$$

Field from which modes can emerge

$$\mathbf{B} = B_z(x)\mathbf{e}_z + B_y(x)\mathbf{e}_y; \qquad \frac{1}{B}\frac{dB_y}{dx} \equiv \frac{1}{L_s}$$

$$\mathbf{k}\cdot\mathbf{B}\left(x = x_0\right) = 0$$

$$\omega_{H*}^2 \equiv \frac{\left(B_y'\right)^2}{4\pi n m_i} k_y^2 \rho_s^2 \qquad \rho_s^2 = \frac{T_{e\|}}{m_i \Omega_{ci}^2}$$

$$\omega_{*e} \equiv -k_y \frac{c}{eB} T_{e\|} \frac{1}{n} \frac{dn}{dx}; \qquad n' \equiv \frac{dn}{dx}$$

$$\omega_{*T} \equiv -k_y \frac{c}{eB} \frac{dT_{e\|}}{dx}; \qquad T_e' \equiv \frac{dT_{e\|}}{dx}$$

$$\alpha_{TL} \equiv \frac{\delta_T^4}{S_L^2}$$

$\mathcal{L} =$ Relevant mode inductivity, $\left(\hat{E}_{\|L} = \mathcal{L} \frac{\partial \hat{J}_\|}{\partial t} \right)$

$$\delta_I^2 \equiv S_L = \mathcal{L} \frac{c^2}{4\pi}$$

Basic Equations for Modes localized Over $\delta_I \equiv S_L^{1/2}$

The four equations in coordinate space are:

$$-\omega\left(\omega-\omega_{di}\right)\frac{d^2\tilde{\xi}_x}{dx^2}=i\frac{\left(\mathbf{k}\cdot\mathbf{B}\right)}{4\pi m_i n}\frac{d^2\tilde{B}_x}{dx^2}, \tag{1}$$

$$\tilde{n}_e=-n'\tilde{\xi}_x-i\frac{ck_\parallel}{4\pi e\omega k_y}\frac{d^2\tilde{B}_x}{dx^2}+i\frac{D_n}{\omega}\frac{d^2\tilde{n}_e}{dx^2}. \tag{2}$$

$$\begin{aligned}\left(\omega-\omega_{*e}-\omega_{*T}\right)\tilde{B}_x=i\left(\mathbf{k}\cdot\mathbf{B}\right)&\left[\left(\omega-\omega_{*e}\right)\tilde{\xi}_x+\omega_{*T}\frac{\tilde{T}_e}{T_e'}+i\frac{\omega_{*e}}{\omega}\frac{D_n}{n'}\frac{d^2\tilde{n}_e}{dx^2}\right]\\&+\omega\left(S_L-\frac{c^2}{\omega_{pe}^2}\frac{k_\parallel^2T_e}{m_e\omega^2}\right)\frac{d^2\tilde{B}_x}{dx^2}\end{aligned} \tag{3}$$

$$D_\perp\frac{d^2\tilde{T}_e}{dx^2}-D_\parallel k_\parallel^2\tilde{T}_e\cong-ik_\parallel D_\parallel T_e'\frac{\tilde{B}_x}{B}, \tag{4}$$

The corresponding equations in Fourier space are, for:

$$\tilde{\tilde{B}}_k \equiv k_y(\tilde{B}_k / B_y') \ \text{ and } \ \tilde{\tilde{T}}_k \equiv k_y(\tilde{T}_{ek} / T_e'),$$

$$\tilde{\xi}_k = \frac{\omega_H^2}{\omega\left(\omega-\omega_{di}\right)}\left[\frac{1}{k_x^2}\frac{d}{dk_x}\left(k_x^2\tilde{\tilde{B}}_k\right)\right], \tag{5}$$

$$\begin{aligned}\left(1+i\frac{D_n k_x^2}{\omega}\right)\tilde{n}_{ek} &= -n'\tilde{\xi}_k - \frac{cB_y'}{4\pi e\omega k_y L_s}\frac{d}{dk_x}\left(k_x^2\tilde{\tilde{B}}_k\right) \\ &\equiv -\left[n'\frac{\omega_H^2}{\omega\left(\omega-\omega_{di}\right)} + \frac{cB_y' k_x^2}{4\pi e\omega k_y L_s}\right]\frac{1}{k_x^2}\frac{d}{dk_x}\left(k_x^2\tilde{\tilde{B}}_k\right)\end{aligned}, \tag{6}$$

$$\left(\omega-\omega_{*e}-\omega_{*T}+\omega S_L k_x^2\right)\tilde{\tilde{B}}_k$$
$$\cong -k_y^2\left[\left(\omega-\omega_{*e}\right)\frac{d\tilde{\tilde{\xi}}_k}{dk_x}-i\frac{\omega_{*e}}{\omega}\frac{D_n}{n'}\frac{d}{dk_x}\left(k_x^2\tilde{n}_{ek}\right)\right]-\frac{c^2}{\omega_{pe}^2}\frac{k_y^2}{L_s^2}\frac{T_e}{m_e\omega}\frac{d^2}{dk_x^2}\left(k_x^2\tilde{\tilde{B}}_k\right) \tag{7}$$
$$-\omega_{*T}k_y\frac{d\tilde{\tilde{T}}_k}{dk_x}$$

$$\frac{d^2\tilde{\tilde{T}}_k}{dk_x^2}-k_x^2\delta_T^4\tilde{\tilde{T}}_k\cong\frac{1}{k_y}\frac{d\tilde{\tilde{B}}_k}{dk_x}. \tag{8}$$

Note that

$$\frac{c^2}{L_s^2}(k_y\lambda_{De})^2=k_y^2\rho_s^2\omega_H^2\equiv\omega_{H*}^2$$

Then,

$$\left(\omega-\omega_{*e}-\omega_{*T}+\omega S_L k_x^2\right)\tilde{\tilde{B}}_k$$
$$\cong -\frac{d}{dk_x}\left\{\frac{\omega_H^2}{\omega+iD_n k_x^2}\left[\frac{\omega-\omega_{*e}+iD_n k_x^2}{\omega-\omega_{di}}\frac{k_y^2}{k_x^2}+k_y^2\rho_s^2\right]\frac{d}{dk_x}\left(k_x^2\tilde{\tilde{B}}_k\right)\right\}-\omega_{*T}k_y\frac{d\tilde{\tilde{T}}_k}{dk_x} \qquad (9)$$

Let us now introduce: $l^2 \equiv k_x^2 S_L$. Thus, $(d/dk_x)=S_L^{1/2}(d/dl)$ and Eq. (8) can be rewritten as

$$\frac{d^2\tilde{\tilde{T}}_k}{dl^2}-\alpha_{TL}l^2\tilde{\tilde{T}}_k \cong \frac{1}{k_y S_L^{1/2}}\frac{d\tilde{\tilde{B}}_k}{dl}, \qquad (8a)$$

where $\alpha_{TL} \equiv \delta_T^4 / S_L^2$.

If, instead of $\tilde{\tilde{B}}_k$, we consider $\tilde{\tilde{B}} \equiv \tilde{\tilde{B}}_k / (k_y S_L^{1/2}) = (L_s / S_L^{1/2})(\tilde{B}_k / B)$, we have

$$\frac{d^2\tilde{\tilde{T}}_k}{dl^2} - \alpha_{TL} l^2 \tilde{\tilde{T}}_k \cong \frac{d\tilde{\tilde{B}}}{dl}, \tag{8b}$$

and Eq. (9) can be rewritten as

$$\begin{aligned} &\left(\omega - \omega_{*e} - \omega_{*T} + \omega l^2\right)\tilde{\tilde{B}} \\ &\cong -k_y^2 \omega_H^2 S_L \frac{d}{dl}\left\{\frac{1}{\omega + i\bar{D}_n l^2}\left[\frac{\omega - \omega_{*e} + i\bar{D}_n l^2}{\omega - \omega_{di}}\frac{1}{l^2} + \frac{\rho_s^2}{S_L}\right]\frac{d}{dl}\left(l^2\tilde{\tilde{B}}\right)\right\} - \omega_{*T}\frac{d\tilde{\tilde{T}}_k}{dl} \end{aligned} \tag{10}$$

where $\bar{D}_n \equiv D_n / S_L$.

Ordering of maximum information:

$\bar{D}_n \sim \omega \sim \omega_{*e}$; $k_y^2 \omega_H^2 S_L \equiv \omega_{H*}^2 (S_L / \rho_s^2) \sim \omega_{*e}^2 S_L / \rho_s^2$, where $S_L > \rho_s^2$.

Modes with phase velocities in the electron diamagnetic velocity direction

Then, considering $\omega = \omega_{*e} + \delta\omega$, where $\delta\omega \sim \bar{D}_n l^2 << \omega_{*e}$, in Eq. (10) we find

$$\begin{aligned} &\left(-\omega_{*T} + \omega_{*e} l^2\right)\tilde{\tilde{B}} \\ &\cong -\omega_{H*}^2 \frac{d}{dl}\left\{\frac{1}{\omega_{*e}}\left[\frac{S_L}{\rho_s^2}\frac{\delta\omega + i\bar{D}_n l^2}{\left(\omega_{*e} - \omega_{di}\right)l^2} + 1\right]\frac{d}{dl}\left(l^2\tilde{\tilde{B}}\right)\right\} - \omega_{*T}\frac{d\tilde{\tilde{T}}_k}{dl} \end{aligned} \tag{11}$$

Next, introduce

$$\eta \equiv \frac{\omega_{*T}}{\omega_{*e}};\ C_* \equiv \frac{\omega_{H*}^2}{\omega_{*e}^2};\ \Lambda \equiv \frac{S_L}{\rho_s^2}\frac{\delta\omega}{\omega_{*e} - \omega_{di}};\ \bar{\nu} \equiv \frac{S_L}{\rho_s^2}\frac{\bar{D}_n}{\omega_{*e} - \omega_{di}} = \frac{D_n}{\rho_s^2\left(\omega_{*e} - \omega_{di}\right)},$$

and rewrite Eq. (11) as

$$\left(l^2 - \eta\right)\tilde{\tilde{B}} \equiv -C_* \frac{d}{dl}\left[\left(\frac{\Lambda}{l^2} + 1 + i\bar{\nu}\right)\frac{d}{dl}\left(l^2\tilde{\tilde{B}}\right)\right] - \eta\frac{d\tilde{\tilde{T}}_k}{dl}. \tag{12}$$

Defining

$$l_*^2 \equiv \frac{l^2}{C_*},\ \eta_* \equiv \frac{\eta}{C_*},\ \Lambda_* \equiv \frac{\Lambda}{C_*},\ \tilde{\tilde{Y}} \equiv \frac{\tilde{\tilde{T}}_k}{C_*^{1/2}} \text{ and } \alpha_* \equiv \alpha_{TL} C_*^2 \tag{13}$$

we finally arrive at the following two coupled equations

$$\left(l_*^2 - \eta_*\right)\tilde{\tilde{B}} \cong -\frac{d}{dl_*}\left[\left(\frac{\Lambda_*}{l_*^2} + 1 + i\overline{\nu}\right)\frac{d}{dl_*}\left(l_*^2 \tilde{\tilde{B}}\right)\right] - \eta_* \frac{d\tilde{\tilde{Y}}}{dl_*}, \tag{14}$$

and

$$\frac{d^2\tilde{\tilde{Y}}}{dl_*^2} - \alpha_* l_*^2 \tilde{\tilde{Y}} \cong \frac{d\tilde{\tilde{B}}}{dl_*}. \tag{15}$$